Three Applications of Satellite-Borne Repeat Pass SAR Interferometry in Southern Africa

Gavin S. Doyle

Declaration

I declare that this dissertation is my own work. it is being submitted for the degree of Master of Science (Applied science) in the faculty of Engineering at the University of Cape Town. It has not previously been submitted for any degree or examination at this or any other university.

Gavin S. Doyle

Acknowledgements

Synopsis

Synthetic Aperture Radar Interferometry (InSAR) is a relatively new remote sensing technique, which can be used to derive precise topographic height and height change information over large areas. It is a technique which has been used in a great variety of situations, from the topographic mapping of Venus to the detection of subtle ground deformations due to earthquakes and mining subsidence.

The InSAR technique involves using the phase information inherent in radar images to extract elevation and elevation change information. The process requires very careful co-registration of a pair of complex images of the same scene, followed by the multiplication of the one image by the complex conjugate of the other. In this manner, a phase image, or interferogram is generated, in which subtle differences in the distances from the two imaging sensors to the ground are mapped, thereby making it possible to generate a height model of the ground surface.

An extension to the InSAR technique, is that of differential InSAR (dInSAR), whereby it is possible to detect changes in elevation over time in the order of a fraction of a wavelength of the radar signal. The signal wavelength of the European ERS sensors, data from which was used extensively in this project, is 56 mm. Any change in the distance from the satellite to the ground of half this distance will cause a phase change of one whole cycle (because of the two-way path of the signal). Hence, each fringe cycle in a differential ERS interferogram represents 28 mm of range change.

The Radar Remote Sensing Group at the University of Cape Town has developed the first viable interferometric processing capability in Southern Africa. An important part of developing this capacity has been the testing of the InSAR technique in real situations. This thesis presents a look at some applications of InSAR and dInSAR to real geophysical and geodetic issues in Southern Africa. It is neither a pure geological nor a pure electrical engineering approach to the subject, but it does endeavor to describe the application of this technology to geophysical and geodetic issues. Three distinct applications are presented, in which the procedures, strengths and limitations of the technique are discussed. The three applications are:

1. The development of a digital elevation model (DEM) of the Western Cape region, using a pair of ERS SAR images.

This project involved applying the InSAR technique to a pair of ERS images to derive a height map of the South Western Cape.

The two images, which were selected from a possible set of five, were selected on the basis of their acquisition times being close together, and their viewing geometry being appropriate for the task. The data selection process for interferometry is critical, as the technique is susceptible to phase decorrelation, which results from a combination of statistically significant changes in the Earth's surface characteristics between image acquisition, and differences in the sensor flight paths.

The images were processed from raw data, and an interferogram was generated. The interferogram, which is a representation of the range difference between the ground surface and the sensors, but with modulo 2π ambiguities, was filtered for noise, and then corrected for the side looking geometry of the SAR sensors. This side looking geometry causes the topographic differences to be superimposed on the differences in range from the near side of the image to the far side. The average component due to the side looking geometry is removed, leaving only that due to topography (and atmospheric effects). The resulting "flattened" interferogram was phase unwrapped where possible, to eliminate the modulo

2π ambiguities. The unwrapped phase image was then used to calculate actual topographic heights, and the resulting height map was then re-sampled and georeferenced so that points on the map could be identified with their corresponding points on the ground.

The phase unwrapping process was incomplete in certain areas of the scene. This was because of information loss due to phase decorrelation in areas subject to radar shadow, layover, and the presence of water bodies. This resulted in there being numerous data gaps in the generated height map. Some of the specific regions affected in this way include all of the dams and reservoirs in the image, most particularly the Theewaterskloof and Steenbras dams. Regions affected by radar shadow tended also to be affected by layover, sometimes eliminating peaks in their entirety from the DEM. The Sentinal, Chapmans Peak, and Hangklip are clear cases of where this happened. Decorrelation due to the effects of wind on vegetation is evident on the slopes of most of the mountains, particularly Devil's Peak, Signal Hill, and the forested areas around Jonkershoek and the Helderberg.

A comparison made between the DEM and independently (optically) derived height information, showed a number of low spatial frequency anomalies in the InSAR derived DEM. The presence of these anomalies has been attributed to refractive variations within the atmosphere at the time of image acquisition. These sorts of aberrations are only prevalent in repeat pass interferometry, where the two images are acquired at different times. It is possible with a dual antenna system, where the antennas are well spaced, to acquire the two images simultaneously, thus eliminating the effects of atmospheric perturbation.

This project was initially intended as a test of the Gamma software suite, but it has become an important demonstration of the effects of atmospheric refraction on the interferometric technique. Work is currently under way to develop techniques for combining multiple data sets, so as to minimise such errors, and to fill the gaps resulting from incomplete phase unwrapping.

2. Katse basin deformation mapping by satellite radar interferometry.

This project involved the use of differential InSAR to map the deformation field associated with the 2 billion tonne load imposed on the Earth's crust by the Katse reservoir in Lesotho. The results were to be used to constrain geophysical models of the Earth's crust in the region, and in so doing, assist reservoir designers in assessing the seismic risk associated with the Lesotho Highlands Water Project.

Predictions, based on an elastic half-space model, indicated that the added load of the water in the Katse reservoir would cause the Earth's crust to be depressed by more than 10 cm. This amount of ground movement is well within the limits of detection by differential InSAR, and the technique had the potential to provide a high resolution map of the deformation and any structural inhomogeneities associated with the loading.

ERS SAR image data of the area was obtained from before, during and after the filling of the Katse reservoir. Where geometric constraints allowed, interferograms were generated, and an attempt was made to produce an InSAR DEM for the purposes of removing the topographic effect from interferograms that should have included the effects of deformation. The alpine type terrain in Lesotho causes significant loss of information in ERS SAR images, mainly through layover and shadow effects. It was therefore not possible to generate such a DEM, and use had to be made of a DEM which was produced by combining an existing, low resolution DEM with one derived by radargrammetrically processing a pair of overlapping images. The viewing geometry used was however inappropriate, and the stereo reduction of a pair of ERS images was only partly successful.

A single interferogram, which included the effects of reservoir loading, was produced from a pair of images acquired with a three year time separation. The fact that it was possible to produce this interferogram represented an indication of the viability of SAR interferometry in areas where the ground surface does not change significantly even over long time periods. The spatial separation of the sensors for this interferogram was small (20 m), and any deformation effects should have been immediately visible, but no such differential effects were apparent. Subsequent to the processing of the interferograms, information obtained from conventional geodetic monitoring of the dam site indicated that the deformation had in fact been almost an order of magnitude less than that anticipated through the elastic half-space modeling. This put the deformation outside the limit of detectability by differential InSAR.

Although no ground deflection was detectable by interferometry, the technique worked far better than expected, given the terrain and time separation between images. This bodes well for the use of this technique in similarly non-ideal conditions.

3. The mapping of ground surface deformations associated with a severe rock-burst in the Welkom gold fields in April 1999.

This project made use of the same techniques as those used in the Katse project, but in much more favorable conditions. The project was concerned with the mapping, by differential InSAR, of the surface deformations caused by an earthquake in the Welkom gold fields in April 1999.

The earthquake caused two fatalities and considerable damage to the Eland shaft of the Matjhabeng mine. The magnitude of the event was measured by seismographs in the area as being M4.5 (local), and was determined to have been induced by the mining activities themselves. Seismicity induced through rockburst is a problem which is becoming more prevalent as mining takes place at deeper and deeper levels. Consequently, it is currently the subject of active research by geophysicists and mining companies. The differential InSAR technique had been used with spectacular success in other parts of the world in mapping deformations due to, among other things, earthquakes and mining induced subsidence. Through this project, it has also been demonstrated to offer valuable input for research into rock failure dynamics in the deep gold mines.

Using combinations of ERS radar images acquired before and after the April 1999 event, a differential interferogram was produced, in which the ground deformation that resulted from the earthquake is very clearly quantified. The result coincides very closely with the location of the fault plane where the movement took place, and also with the mine shaft where the worst of the damage was reported.

Contents

List of Figures

List of Tables

Glossary and Definition of Acronyms

Ascending pass: South to north relative orbital direction of satellite.

Azimuth: The along-track direction in SAR imaging.

Backscatter: Radar signal energy scattered back towards the instrument.

Baseline: The vector separation, or distance between two orbital trajectories.

C-band: Radar frequency around 5GHz.

CEOS: Committee on Earth Observation Standards

Coherence: The degree of phase similarity between pixels in different images.

Corner reflector: A trihedral target made from aluminium or steel and oriented on the ground toward the radar to provide a bright pixel for image intensity calibration.

DEM: Digital Elevation Model - Terrain height data represented digitally on a regular grid.

Descending pass: North to south relative orbital direction of satellite.

dInSAR: Differential interferometric synthetic aperture radar.

DLR: Deutsche Forschungsanstalt für Luft und Raumfahrt (German Aerospace Research Establishment).

DWAF: South African Department of Water Affairs and Forestry.

Ephemeris: A set of *state vectors* used to calculate the path traveled by a spacecraft.

ERS-1 & 2: Earth Resource Satellites 1 and 2. ESA satellites carrying, among others, SAR instruments.

ERS Tandem: SAR acquisitions of the same scene by ERS 1, followed 1 day later in the same orbit by ERS 2.

ESA: European Space Agency.

ESRIN: The European Space agency's centre in Frascati, Italy.

Feathering: A technique used in *mosaicing* to reduce the discontinuities at seams between component images

Foreshortening: The apparent spatial compression in the image of slopes facing the radar.

Gamma software: A suite of processors for SAR applications.

Geocoding: Geometric correction and registration of an image to map co-ordinates (often involves orthorectification).

GPS: Global Positioning System. (US military satellite constellation providing real-time positioning data).

Ground truth: Observations relating real phenomena to corresponding features in a remotely sensed image.

L-band: Radar frequency around 1.2GHz.

Layover: Extreme form of foreshortening in which the top of a reflecting object (such as a mountain) is nearer to the radar (in slant range) than the lower parts of the object are. The image of such an object appears to have fallen over towards the radar.

Mosaicing: The process of merging overlapping sub-images to form a larger, single image.

Multi-look image: Image resulting from a process in SAR by which the full synthetic aperture is split into several sub-apertures, each representing an independent "look" of the identical scene. The resulting image formed by incoherent summing of these "looks" is characterised by reduced *speckle* and degraded spatial *resolution*.

Orthorectification: Correcting image distortions which are due to terrain effects.

Range: The distance between sensor and target. Also the direction perpendicular to the sensor flight direction.

Resolution: The ability to distinguish between objects on the ground. Also, the 3dB (power) width of the impulse response.

SAC: Satellite Applications Centre (CSIR subsidiary)

SAR: Synthetic Aperture Radar

Shadow: Areas in an image where steep terrain blocks the radar beam. Only noise values appear in these pixels.

SIR-C: Shuttle Imaging Radar C.

Slant range: The distance from radar to target.

SLC: Single Look Complex (SAR image data with phase information preserved).

SLR: Satellite Laser Ranging (The use of Lidar to determine location and acceleration of satellites)

Speckle: Spatially random multiplicative noise due to coherent superposition of multiple backscatter sources within a SAR resolution element.

SRTM: Shuttle Radar Topographic Mission.

State vector: An array containing a spacecraft's location, velocity, and acceleration at a particular time.

Swath: The strip of ground imaged by an orbiting sensor.

Tie-point: A recognisable feature on the surface which can be related geographically to an image or between images.

Chapter 1

Introduction

Interferometric Synthetic Aperture Radar (InSAR) is a relatively new remote sensing technique for deriving terrain height and very subtle height change information. Although it is a technique which is well established in the realms of research, it hasn't quite emerged yet into regular commercial use. This is largely due to there being a number of prerequisite conditions for its viability in any given situation. As a consequence of these conditions, the selection of suitable data is not straight forward, and appropriate data is sparse. This situation is changing, as large volumes of global data are continually being archived, thus increasing the pool from which to draw data suitable for interferometry.

Since the mid eighties, Synthetic Aperture Radar (SAR) interferometry has been put into practice with widely varying degrees of success. A great many applications have been written about in various scientific journals, particularly in the fields of geology and glaciology. There is a natural bias in the number of published works, towards those projects that achieved success. Failures are not often reported on. It is therefore very difficult without first hand experience to determine the robustness and applicability of a technique which has not yet reached the domain of commercial applicability.

This thesis represents a report on three real applications of InSAR. Although the fundamental technique, which will be discussed in the earlier chapters, is the same for all of them, the aims, the processing methods and the results of each application are presented separately. These application areas are:

1. The production by InSAR of a digital elevation model of the South Western Cape.

Using the InSAR technique, either with dual antenna systems, or with two or more passes over the same area, it is theoretically possible to produce detailed and accurate three-dimensional relief maps of the Earth's surface. As a means of testing the "repeat pass" InSAR technique, a pair of ERS radar images were used to derive a DEM of the South Western Cape. A brief description is given of the procedures followed when using the Gamma® processor, of some of the difficulties that were encountered, and how some of them were overcome.
Some of the drawbacks to InSAR DEM production in mountainous areas are discussed, as well as issues relating to atmospheric perturbations, which adversely affect repeat pass interferometry. Some suggestions and recommendations are given for improving InSAR DEM production.

2. An attempt at measuring crustal deflection due to reservoir loading in Lesotho.

This was an ambitious experiment which involved using differential InSAR to measure and map the flexure of the Earth's crust due to the filling of the Katse Reservoir in Lesotho. The results were to be used to model the rheological properties of the Earth's crust in the region as a whole. In particular, a value for the flexural thickness of the crust was to be derived, and used to more accurately assess the seismic risk associated with the Lesotho Highlands Water Project.
Early predictions, based on an elastic half-space model, suggested that the added load of the water in the Katse reservoir would cause the Earth's crust to be depressed by more than 10

cm. This amount of ground movement is well within the limits of detection by differential In-SAR, but the terrain and the long time period over which the experiment was conducted were expected to be limiting factors from the outset. Although no ground deflection was detectable by interferometry, the technique worked far better than expected, given the terrain and time conditions. The amount of actual crustal deflection, as measured by standard geodetic methods, was almost an order of magnitude less than that predicted by the model, and was outside the limit of detectability by InSAR.

3. Mapping the ground surface deformation due to and earthquake in the Welkom area.

In April 1999, an earthquake caused considerable damage and two fatalities in the gold mining area of Welkom in the Free State province of South Africa. This seismic event, with a magnitude (local) of 4.5, was induced by the mining activities themselves. This problem of induced seismicity through rockburst is one which is becoming more prevalent as mining takes place at deeper and deeper levels. The cost in terms of human life and productivity loss is of grave concern, and this issue is currently the subject of active research by geophysicists and mining companies. Given that the differential InSAR technique had been used with spectacular success in mapping earthquakes and also mining induced subsidence in other parts of the world, we felt that it might also offer valuable input for research into rock failure dynamics in the deep gold mines.

Using combinations of ERS radar images acquired before and after the April 1999 event, we were able to derive a map of the ground deformation that resulted from the earthquake. The result coincides very closely with the location of the fault plane where the movement took place, and also with the mine shaft where the worst of the damage was reported.

Chapter 2

Background and Theory

2.1 Principles of radar imaging and interferometry

2.1.1 Synthetic Aperture Radar (SAR)

Airborne or space-borne real aperture and synthetic aperture imaging radars are both side looking active radar sensors. They are pulsed systems that make use of the range gating technique to obtain image resolution in the range, or across track direction (Figure 2.1). Since, for a given wavelength, λ, the angular beam width (Θ_{BW}) is inversely related to antenna size (L_A), a real aperture radar has to rely on a physically large antenna to obtain good azimuth resolution (equation 2.1) [1][2].

$$\Theta_{BW} = \frac{\lambda}{L_A} \tag{2.1}$$

For the altitudes at which satellites operate (at frequencies between 1 and 10 GHz), the size of antenna required for reasonable real aperture azimuth resolution would be impossible to produce let alone put into orbit. So, in order to attain the required azimuth resolution, synthetic aperture radar (SAR) takes advantage of a physically small antenna and of the Doppler history of the radar echoes generated by the forward motion of the platform to *synthesise* a large antenna during reconstruction of the image. At a slant range of approximately 800km, the real aperture azimuth resolution of the ERS-2 SAR, which has a 12m antenna, is approximately 3km. With aperture synthesis, a resolution of only 10m is attained.
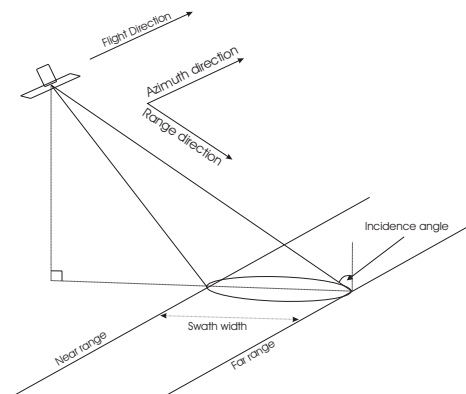
Figure 2.1: Imaging radar geometry

Because the beam width in the along track direction is finite, the radar is not strictly only a side looking sensor. A portion of the beam will be looking slightly ahead of it, and a portion slightly behind. The result of this is that the returned signal is Doppler shifted by an amount related to how

16

far fore or aft the target is at any given moment. In other words, if one considers a scene containing a single bright target, by tracking its Doppler history and its range (which will decrease and then increase again as the sensor moves past it), it will be possible to focus the return signal to a point, thus improving the azimuth resolution. A further advantage to aperture synthesis is that a very high signal processing gain results from the coherent, or range correlated summation of the signal returns.

2.1.2 Interferometric SAR (InSAR)

The backscattered radar signals are separated into In-phase and Quadrature (I and Q) components prior to sampling. From the I and Q components of the signal, the amplitude and phase can be determined as $\sqrt{I^2 + Q^2}$ and $\arctan\left[\frac{Q}{I}\right]$ respectively. Interferometric synthetic aperture radar makes use of this phase information in two or more complex SAR images to extract information about the Earth's topography.

A Single Look Complex (SLC) radar image is nothing more than an array in which the I and Q values for each pixel, or resolution element in slant range have been preserved. An SLC image is usually presented as a dual band (I and Q) 32 bit float, where the bands are interleaved by pixel (BIP). Typical radar images (multi-look intensity images) display only amplitude data. SAR interferometry makes use of the coherent nature of the radar system, using the phase measurements to infer differential range and range change in two or more SAR images of the same surface. By this technique, multiple SAR images of the same scene can be used to detect very small (1 cm or less) surface elevation changes over large areas [3]. This technique, which in the case of the ERS data being used in this particular study, and which after multilook processing and slant to ground range conversion, has a spatial resolution of about 25 m, is sufficiently sensitive for it to be used in the monitoring of subtle crustal motion.

InSAR Imaging geometry

In repeat-pass InSAR, the interferometric baseline, B, is defined as the cross-track orbit separation, or the distance perpendicular to the satellite flight direction between two repeat orbits. In the estimation of topographic elevation by InSAR [4][5], one can consider the geometry illustrated in Figure 2.2, where $A1$ and $A2$ are two radar antennas which simultaneously view the same point $z(y)$ on the surface (Antenna $A1$ transmits and receives, whilst antenna $A2$ only receives). The two antennas are physically separated by a baseline vector B, which has length $\mid B \mid$ and angle α with respect to the horizontal. $A1$ is at height h above some reference datum (generally the WGS84 ellipsoid in the case of satellite interferometry). The range from $A1$ to point $z(y)$ is ρ, and the range from $A2$ to point $z(y)$ is $\rho + \delta\rho$.
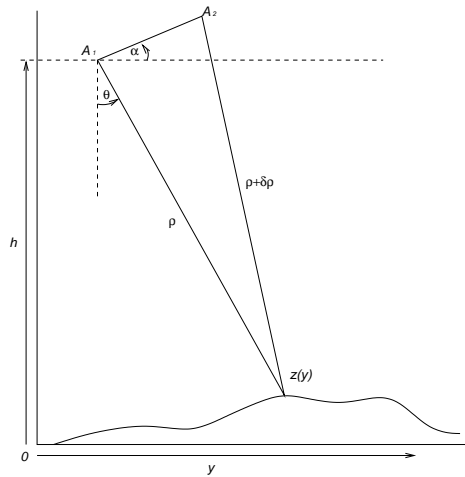
Figure 2.2: InSAR imaging geometry - $A1$ and $A2$ represent two radar antennas viewing the same surface simultaneously, or a single antenna viewing the same surface on two separate passes.

The difference in phase angle between the signal received at $A1$, and the same signal received at $A2$ is a function of both the viewing geometry and the height of point z above the datum. If the viewing geometry is known, then the topography $z(y)$ can be inferred modulo 2π (a phase measurement of θ radians is indistinguishable from a measurement of $\theta + 2n\pi$ radians) from the phase measurement in equation2.2:

$$z(y) = h - \rho \cos \theta \tag{2.2}$$

where θ = radar look angle.

Also,

$$
\begin{aligned}
(\rho + \delta\rho)^2 &= \rho^2 + B^2 - 2\rho B \cos\left(\alpha + 90 - \theta\right) \\
&= \rho^2 + B^2 + 2\rho B \sin\left(\alpha - \theta\right) \\
\sin\left(\alpha - \theta\right) &= \frac{(\rho + \delta\rho)^2 - \rho^2 - B^2}{2\rho B}
\end{aligned}
$$

The phase difference φ between the two receiving antennas is directly proportional to $\delta\rho$ such that

$$\varphi = \delta\rho \frac{\lambda}{2\pi} \tag{2.3}$$

where λ is the transmitted signal wavelength. Hence, the value of φ is only known modulo 2π, and phase unwrapping is required to determine the integer number of wavelengths within $\delta\rho$ [6].

Expressing the topography $z(y)$ in terms of the measured phase and system geometry, we have:

$$z(y) = h - \left\{ \frac{\left[\left(\frac{\lambda\varphi}{2\pi}\right)^2 - B^2 \right]}{2B \sin\left(\alpha - \theta\right) - \left(\frac{\lambda\varphi}{2\pi}\right)} \right\} \cos\theta \tag{2.4}$$

where the value of $z(y)$ represents an average height within a resolution element or pixel.

2.1.3 Repeat pass interferometry

With the exception of the recent SRTM mission, space-borne SAR platforms have all been single antenna systems, and as such are not capable of simultaneous acquisition of the image pairs required for interferometry. So, instead of using two antennas concurrently, it is necessary to obtain interferometric phase measurements by using a single antenna system that images the same area on the ground from the same position in space, but at different times. This is known as repeat pass interferometry, which makes use of the orbital periodicity of satellites. In this case, since each antenna acts as transmitter and receiver, there is a factor of 2 difference in equation 2.3, which becomes:

$$\varphi = \delta\rho \frac{\lambda}{4\pi} \tag{2.5}$$

As with dual antenna systems, accurate knowledge of the baseline length and orientation is of fundamental importance. Satellites such as ERS-1 and ERS-2 are tracked by several means, including on-board GPS and satellite laser ranging (SLR) and relative antenna positions can be determined to within 5mm accuracy. This is of sufficient accuracy for an absolute topographic height determination of about 2m [5].

2.1.4 Differential interferometry

There are a number of ways in which differential interferometry (dInSAR) can be achieved. All of them involve the separation of the signal's phase component due to surface or propagation changes from that due to topography. Commonly, the topographic phase component is extracted by means of simulation of an interferogram from an existing DEM. This interferogram would be simulated with the same imaging geometry as that for the real image pair.

A phase comparison can also be performed between the interferogram created by the two images, and a third image acquired at a later date. If, between the earlier acquisitions and the later one, ground surface movement has taken place, a differential, or double-difference interferogram can be formed by differencing the phase returns. This differential phase contains information regarding the change in range to the antenna, and it can be used to determine ground elevation change to within a fraction of a radar wavelength (5.6cm in the case of ERS).
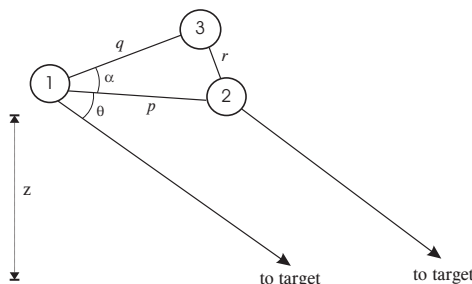
Figure 2.3: Imaging geometry for three pass differential interferometry - Three observations of the same scene are made from three locations in space, separated by baselines p, q and r

Figure 2.3 represents the antenna geometry of three successive data takes of the same scene. Since the resultant phase associated with a given pixel is given by equation. 2.5, and the phase difference between the first two observations is:

$$\triangle\varphi_{12} = (4\pi/\lambda)p\cos\theta \tag{2.6}$$

and the phase difference between the first and third observations is:

$$\triangle\varphi_{13} = (4\pi/\lambda)q\cos(\theta + \alpha) \tag{2.7}$$

The amount by which the two phases $\triangle\varphi_{12}$ and $\triangle\varphi_{13}$ differ can be expressed as:

$$\Phi = \triangle\varphi_{12}/q - \triangle\varphi_{13}/p + c \tag{2.8}$$

It is apparent from this relationship that ambiguities exist in the case of there having been surface changes between the acquisition of images 1 and 2, (thereby changing $\triangle\varphi_{12}$), or may have occurred in the opposite direction between acquisitions 1 and 3 (changing $\triangle\varphi_{13}$). In either case, the best solution is to make use of ground control points, which can be independently surveyed. As is the norm with any such construction, survey monuments have been placed around the Katse dam, and these are being monitored by conventional or GPS geodetic techniques.

2.2 Practical aspects of interferometry

There are numerous factors that affect the feasibility and accuracy of InSAR DEM production or surface change detection. These factors have to be borne in mind when selecting data.

2.2.1 Baseline selection

For InSAR, the critical parameter is the perpendicular baseline, $B_\perp$, which is the component of the baseline which is perpendicular to the SAR slant-range direction. For InSAR to be possible, $B_\perp$ has to satisfy conditions determined by the radar characteristics and the imaging geometry. The image cross correlation fall-off due to increased baseline length is a function relating to the spectral shift of the signal from one image to the other. This shift is due to the slight difference in local incidence angles [4], and for the ERS system, the theoretical upper limit of $B_\perp$ is 1 100 m. By referring to Figure 2.4, it will be noted that for practical purposes, if sufficient phase coherence is to be maintained between the two images, the baseline should be less than about 500 m for flat terrain. On the other hand, in order that the interferogram fringe rate (Figure 2.5) is sufficient for the mapping of topography, the baseline should not be close to zero. If the baseline is zero, any phase difference between the images must be due to ground deformation, (or changes in atmospheric conditions between the two acquisition times). Low values of $B_\perp$ ($<$ a few metres), well suited to the detection of surface feature movement, but not practical for topographic mapping
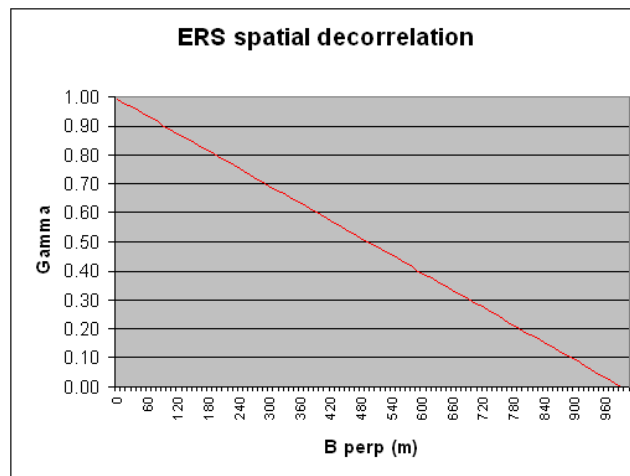
Figure 2.4: Phase coherence between ERS data sets as a function of baseline length alone

2.2.2 Temporal decorrelation

The baseline criterion, even if satisfied, is not a sufficient condition for the InSAR technique to be possible. A further factor affecting the coherence between SAR images, and one to which dual antenna systems are not susceptible, is something known as temporal decorrelation. This is a phase decorrelation caused by random change, between image acquisitions, in the scattering statistics both within individual resolution cells, and in the scene as a whole. This is usually caused by changes in the surface characteristics, such as vegetation growth or movement of any kind.

The resultant phase angle for a single pixel is the vector sum of the contributions from all of the scatterers within a single resolution element. So, if between passes, the relative positions of the scatterers within a pixel change by an amount greater than the radar wavelength ($\lambda = 5.6$ cm, ERS sensors), then phase coherence will not be maintained in the second image relative to the first. A phase comparison can then not be performed, and all topographic information will be lost. This type of decorrelation can take place over time spans as short as a few hours in windy vegetated regions. In dry, desert regions on the other hand, good phase correlation can be maintained over several months or even years. If the change is over a large area, with coherence being maintained within the pixels, and over several adjacent pixels (the entire ground surface has moved), and the flight path has repeated itself exactly, the phase difference will be related to the magnitude of the ground movement. With a nonzero baseline however, the phase difference due to surface changes becomes scrambled with the topographic information, necessitating a third observation. Because of the heavy summer rains and heavy winter snow-falls in the Lesotho, temporal decorrelation due to changes in the surface

(a) Example of fringe rate due to a 160m baseline

(b) Example of fringe rate due to a 92m baseline

Figure 2.5: Differences in fringe-rate in the Katse region resulting from different baseline lengths.

characteristics over the long time periods that this project was likely to have to contend with, were our biggest concern with regard to the viability of the technique.

2.2.3   The ERS system

The ERS system comprises two single antenna satellites, ERS-1 and ERS-2, in near polar orbit at a nominal altitude of 785km (Because of the failure of its power system, ERS-1 had since ceased operating). The SAR instruments are right looking, with a swath width of 100km, and a centre-swath incidence angle of 23º. They are C-band instruments, with a centre frequency of 5.3GHz.

The ERS satellites are susceptible to orbit deterioration through air drag effects, and the gravitational influence of the Sun. This gravitational effect, which is seasonally variable, results in an orbital inclination drift, whereby the satellite in near polar orbit tends to precess towards an equatorial orbit. Another, and more important reason from our point of view, is that of the requirements for repeat pass interferometry. For reasons stated above, for interferometry to be viable, the orbital separation, or baseline, must be kept well within 1km.

2.2.4   Geometric considerations

The ERS system has a nominal incidence angle of 23º, and is thus not ideal for use in mountainous areas. The steepness of this angle is such as to cause considerable layover in regions of high relief. On the other hand, this steep incidence angle minimises the amount of shadow caused by steep slopes on the "leeward" side of the imaging system. For DEM production, a larger incidence angle should ideally be utilised, and the scene should be imaged interferometrically from both sides, thus allowing for the combination of the resultant DEMs.

2.2.5   Flat Earth phase removal

Because a SAR is a side looking instrument, and there is a difference in range from the "near" side to the "far" side of the scene, an almost linear phase component is introduced into the interferogram. This phase component, the flat Earth component, has to be subtracted from the interferogram so that the remaining fringes are due to topographic variation alone. The flat Earth fringe rate varies as a function of baseline length (a zero baseline interferogram will only include fringes due either to ground surface movement between acquisitions, or to atmospheric effects).

The removal of the flat Earth phase component can be achieved either by retrospective processing of the interferogram, using the Fourier transform method to estimate the average fringe rate across the image, or by derivation from the imaging geometry. The first method assumes that there is no regional slope across the image scene, and the second method requires that the orbital ephemeris information is accurate.

2.2.6   Ephemeris data

The processing of SAR data requires that the sensor positions and velocities be accurately recorded for the duration of the image acquisition. This is primarily so that the images can be focused accurately, but it is also required for image registration and for coarse baseline estimation. The satellites have on-board GPS for recording this information, but the accuracy is often not sufficient for precise interferometric work.

By employing a number of techniques, including Satellite Laser Ranging (SLR) and geoid modeling, improved orbital statistics are acquired and recorded by various institutions, including the DLR, TU Delft (Delft University of Technology) and ESA. SLR is achieved by "firing" a pulsed laser at the satellite (which is equipped for such purposes with a retro-reflector), allowing for precise position and trajectory determination. There are only a few of these SLR stations around the world, so a certain amount of interpolation is required, particularly in the Southern Hemisphere. The interpolation methods require accurate modeling of the Earth's geoid or gravity field. The precise orbit data, which can be accessed at the DLR by prior arrangement, are simple listings of state vectors, or points through which an orbital trajectory will be interpolated.

2.2.7 Atmospheric effects

The effects of ionospheric scintillation on radar signal propagation, such as attenuation, phase shift, dispersion and refraction, are well known. The consequences for InSAR of these perturbations are however regarded as being insignificant. The reason for this is that the scale, or extent of the perturbations is generally so large as to impart a uniform shift between image acquisition. After interferometric processing, such a shift would be indistinguishable from that caused by an error in baseline estimation, and so can be ignored. Difference mapping in SAR interferometry is only viable for changes which have a lateral extent less than the imaged area. The possible unpredictable effects of localised atmospheric vapour and temperature variations [7] are of grave concern in repeat pass interferometry, however, particularly as the Lesotho region is mountainous, and prone to orographic weather conditions.

The effects of atmospheric perturbations is discussed in Chapter 3, which pertains to the generation of a DEM by means of Tandem ERS data from the Western Cape area.

2.2.8 Independent DEM requirements

In the differential InSAR process, it is possible, and sometime necessary to use a DEM from an independent source for the removal of the effect of topography on the interferogram. The coarseness of resolution and the vertical accuracy of this is not as critical as one might intuitively think. This is discussed succinctly by Massonnet and Feigle [6]. The interferometric fringe rate, or topographic height ambiguity is described by equation 2.9:

$$h_a = \frac{R_s \lambda \tan \theta_n}{2d} \tag{2.9}$$

where R_s is the range from the satellite to the ground (nominally 800km for ERS), λ is the radar wavelength (56mm for ERS), θ_n is the nominal incidence angle (23º for ERS), and d is the perpendicular baseline.

As an example, if one considers the case of a 20m baseline with ERS data, a situation that presented itself with a pair a Katse images with a three year separation.

In this case, $h_a = 475$m

What this implies is that the fringe rate is equivalent to one interferometric fringe every 475m of topographic variation. As a corollary to this; if we were to use an inaccurate DEM for removal of the topographic component in a differential analysis, the inaccuracies would have to exceed 475m to cause residual topographic fringes to appear in the differential interferogram. Furthermore, these residual fringes would be unlikely to correspond with the location and shape of the expected deformation. The residual, finer detail of the topography will remain in the difference map, but it will follow or conform with the topography, and should be clearly distinguishable from any differential effect.

2.2.9 Linear phase ramps in differential data

Linear ramps in interferograms are the result of incorrect "flat Earth" phase removal. The "flat Earth" phase component results directly from the side-looking imaging geometry, and presents itself as a regular, straight fringe pattern across the whole scene, and on top of which the topographic phase components is superimposed (Figure 2.6 (a)). The flat Earth component is is calculated using a baseline estimate derived either from the orbital state vectors or by means of a Fourier transform of the interferogram. It is then removed from the interferogram so as to leave only the topographic (and differential) fringe component (Figure 2.6 (b)). If the baseline estimation is in error, a residual "flat Earth" component will remain, causing a linear ramp in the "flattened" interferogram.

The only sure way to estimate the baseline with sufficient accuracy to eliminate any residual phase ramp is with the aid of accurate ground control points in both the near and far range regions of the scene. An example of the effect of a residual flat Earth component is discussed in chapter 3

(a) Unflattened interferogram (92m baseline)

(b) Interferogram (92m baseline) flattened by subtraction of average fringe rate.

Figure 2.6: Interferogram "flattening" by subtraction of average fringe rate.

Chapter 3

InSAR DEM construction for the Western Cape - A case study

3.1 Introduction

An accurate knowledge of the shape or form of the Earth's surface is a fundamental requirement of a multitude of disciplines. For example, in order to plan the route taken by a new road through a mountain range, or the positioning of a dam, civil engineers require an accurate model of the terrain. Digital terrain, or digital elevation models (DEMs) are also used in the efficient positioning of radio or cell phone transmitters. Geologists require an accurate knowledge of the surface morphology in order to project exposed structures into three dimensions, thus building models of sub-surface geology. Military applications include the pre-launch programming of cruise missiles with digital terrain data, so that they can maintain a "ground hugging" flight path, and thus avoid detection. Hydrologists also require high resolution, accurate height maps of the ground's surface, in order to predict run-off characteristics. The improvement of digital terrain data is constantly being encouraged by all of these disciplines and more.

The more traditional methods used in the production of DEMs usually involve the use of photogrammetric techniques, which make use of parallax differences between aerial photos or optical satellite images of the same scene, but obtained from slightly different positions. Although the photogrammetric technique is reliable in terms of gross errors, the precision with which elevations can be measured is often insufficient for the required application. Furthermore, the resolution, or sample spacing, of these DEMs is often too coarse. SAR interferometry can potentially provide an alternative, or at least supplemental, means of DEM generation. In the case of ERS interferometry (a repeat pass system), it is possible to obtain spatial resolutions of 25m (interferogram multi-looked 5 times in azimuth), and precision which is dependent on terrain variability and on sensor geometry (a longer baseline causes a higher fringe rate, and consequently a higher sensitivity to terrain height variation). There are practical aspects of InSAR DEM production that can seriously limit the accuracy and reliability of the product however. The distinction between precision and accuracy is critical here. No matter how a DEM is derived, the accuracy of the product will depend largely on the quality and distribution of ground control, and on systematic limitations.

The aim of this study was to generate, using the InSAR technique, a DEM for a geographic region that is varied in terms of its topography and ground cover, and for which other data sets and personal knowledge were available. A pair of ERS SAR images of the South Western Cape (Figure 3.1) were processed from raw data and used to generate a height map using the interferometric method. This DEM was then compared with alternative survey data and evaluated for errors and aberrations (section 3.5).
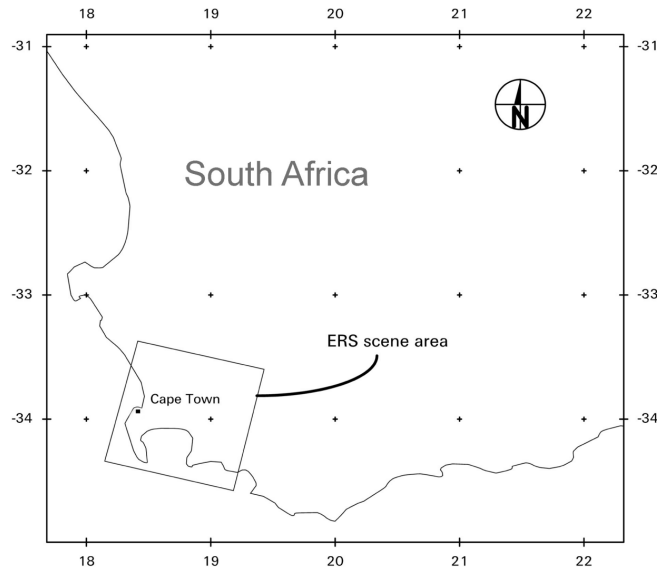
Figure 3.1: Location map indicating area of study

3.2 Site selection

The South Western Cape, including Cape Town itself, (Figure 3.1) was selected as the study area. This locality, (Figure 3.1 and Figure 3.9) is such that within the scene, there are regions of radar shadow, layover, urbanised terrain and also vegetated areas. Partly because of this terrain variability, this was deemed to be a good test site for InSAR DEM production. The scene also contains a substantial length of coastline (over 200km), which represents an excellent datum for phase unwrapping.

Much of the area is represented by a broad tombolo, joining what is now the Cape Peninsula, to the hinterland. This extremely flat and low-lying area, known rather unsurprisingly as the Cape Flats, has an average elevation above sea level of not more than about 20m. The surrounding mountains rise rapidly to 1 800m or more (elevation of Table Mountain ~1000m).

3.3 Data selection

Because of the lack of availability of a dual antenna SAR system, use was made of a pair of images that were acquired during the first ERS Tandem mission in May 1996. This was a special interferometric acquisition phase, during which the orbits of the two ERS satellites were trimmed to within 1 km of each other. The ERS-1 acquisitions were followed one day later, in approximately the same track, by ERS-2 acquisitions, thus generating repeat pass interferometric data sets with good baselines and a short temporal difference.

The selection of specific images is done by means of the ESA-Eurimage Descw software[1]. Essentially what Descw provides is an intuitive, graphical means of searching the ESA image database. The required satellite parameters are entered in the search criteria. These include fields such as acquisition period, whether one wants only Tandem pairs, whether either or both ascending or descending orbits are acceptable, and of course, one's geographic region of interest. Descw then searches the database and provides a list of images that have been acquired (or are due to be acquired), together with a graphical display of the relative baselines. A weekly update of the database is provided for download from ESRIN.

For this study, the search parameters entered were such that only ERS Tandem data over Cape Town was searched for. It did not matter that the data might be three or four years old, so long as the

---

[1]Software utility provided by the European Space Agency as a free download from ESRIN http://earth1.esrin.esa.it/eeo/rgt/installdescw95

baselines were sufficiently short for interferometry to be viable. The results of the search are presented in table .

Track: 0350
Frame: 4293

	Mission	Date	Orbit	$\mathbf{B}_\perp$	$\triangle$ Days
1	ERS-1	1995-11-30	22883	363	176
2	ERS-1	1996-05-23	25388	87	1
3	ERS-2	1995-12-01	3210	340	175
4	ERS-2	1996-05-24	5715	0	0

Images 2 and 4 were selected

Table 3.1: Tandem ERS images available for Western Cape DEM production.

Two pairs were available; one with a 23 m baseline, and the other with an 87 m baseline. Interferograms generated from image pairs with short baselines have a low fringe rate, and are sensitive to differential changes in the ground surface. Longer baselines make for a higher fringe rate, and a higher sensitivity to topographic variation. For this reason, the pair with the 87 m baseline was selected. The month of acquisition was May, which is generally a dry month, and one in which agricultural crops are in a fallow state, decorrelation effects were not expected to be a problem.

3.4 Data processing

All of the processing for this study, apart from the product evaluation, was done using the Gamma® suite of processors. The evaluation of the resultant DEM was done using ERDAS Imagine.

3.4.1 Processing steps in brief

The InSAR processing steps are summarised with comments as follows (Figure 3.2):

1. **Acquire two images** of the same scene. (either dual antenna or repeat pass) with suitable baseline.

   Having selected and obtained the raw SAR data, each of the processing steps is accomplished with the Gamma® modular processor. Refer to the appendices for example scripts that also serve to describe these processing steps.

2. **Form two single look complex SAR images**.

   The Gamma processor uses parameter files, (Appendix F), which provide all of the relevant details for generation of SLCs and interferograms. The processing parameter files are derived from information in the leader files, which accompany the raw data on the CD or tape. It is not unusual, because of the wide variety of CEOS formats, that difficulties will be encountered when reading these leader files. They are mixed binary and ASCII files, which are incorrectly read by the extraction software if there is a single byte missing or out of place. These problems were encountered in the case of this study, and it was necessary to manually correct errors derived from header inconsistencies. An example of a complete leader file, as generated at the Satellite Applications Centre (SAC), and extracted to ASCII text, is presented in appendix E. Obvious errors have been high-lighted

   The use of precise orbit data is not mandatory, but it is recommended for interferometric work. The precise orbit data was used for this study, replacing the state vectors in the Gamma parameter files.
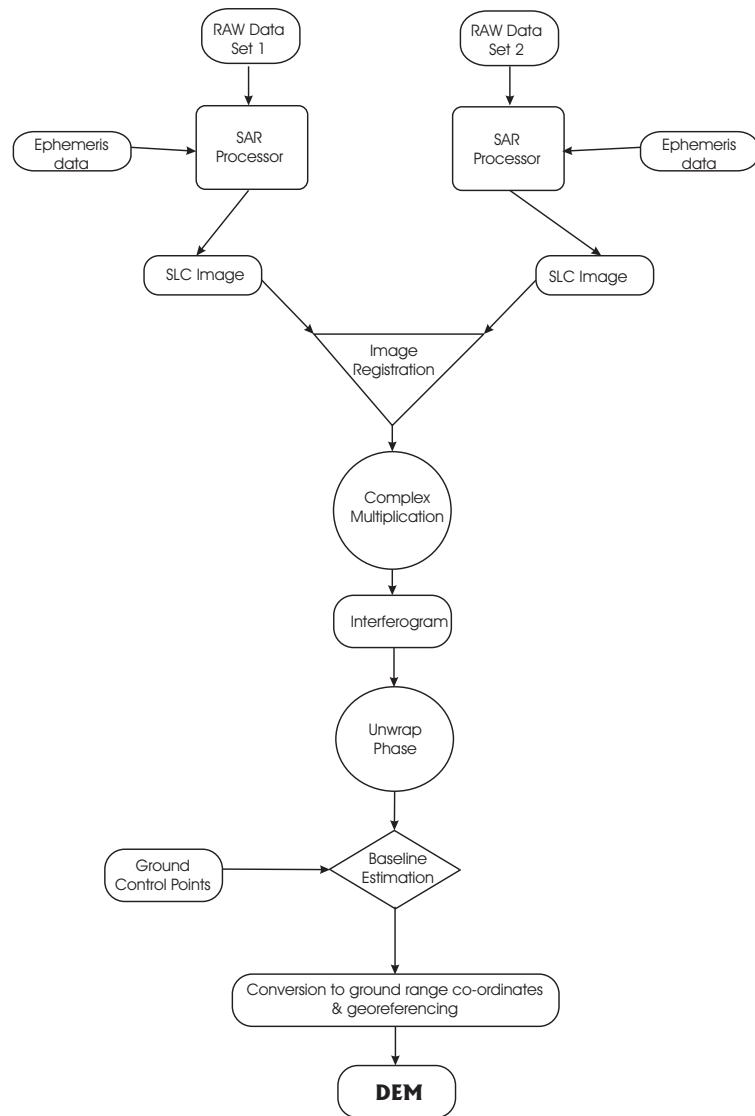
Figure 3.2: Flow diagram showing processing steps for DEM production

The missing line detector was run with the cross-correlation analyser turned off. This routine is designed to detect repeated lines, and its use is not appropriate with ERS data, as the ERS system line counters are reliable.

3. In order to **assess the quality of the SLC** that has been produced, a multi-look intensity image was generated from each SLC. One of them is presented in Figure 3.9.

4. **Register the images** accurately.

5. **Produce the interferogram** (Figure 3.5) by complex multiplication of the two images.

6. **Unwrap** the resultant phase.

   Phase unwrapping in the Gamma processor is achieved by means of a region-growing algorithm. The operator manually selects the point from which unwrapping should be initiated. If unwrapping is unsuccessful, the procedure should be restarted from a different position. The selection of the starting point is based on the coherence of the point and its surrounding pixels. The coherence should be high.

   It is possible to create "bridges" to assist the unwrapping process. These bridges should tie points of equal phase (an unwrapped point to a still-to-be unwrapped point).

7. **Convert unwrapped phase to heights in ground range**

   This is an important step, in which the unwrapped phase is converted to real height values and the DEM is georeferenced. This involves a slant to ground range conversion and an accurate estimation of the baseline. Baseline estimation is accomplished with the assistance of at least three ground control points. These ground control points, which are points with known location and height, should be located in regions of high coherence, and as far apart as possible.

3.4.2 Some comments on processing

In the phase unwrapping stage, there are many variables and combinations of variables that can be adjusted in order to facilitate the process. These parameters include the setting of correlation thresholds, layover region masking, seed position selection, and others. All of these variables and thresholds are set as trade-offs against one another, and inappropriate settings can introduce intrinsic errors which may not be easily detected.

3.5 Results and quality assessment

Although the results of this study may appear somewhat disappointing, it should be noted that there are numerous ways in which they can be refined. These will be discussed later.

Much of the Cape Flats is urbanised, and provides good phase coherence between the two images. The mountainous regions on the other hand, are vegetated with a shrub type vegetation known as vynbos. As may be inferred from the state of the sea in the intensity image (Figure 3.9), the conditions were very windy during the acquisition of at least one of the images used in this study. Such conditions are conducive to decorrelation in vegetated areas, and this decorrelation is evident particularly on the hillside above the city of Cape Town (Figure 3.4).

Due mainly to the large amount of layover in the mountainous regions, a significant portion of the interferogram could not be phase unwrapped. There are non-contiguous "patches" of interferogram in these areas that can be independently unwrapped, but there would be no way, without good ground control, to connect them to one another without inducing gross errors.

Perhaps the most significant feature in the DEM is that of what appears to be due to atmospheric aberrations. A broad, periodic, south-west/north-east striping, with a wavelength of 5.5km and amplitude equivalent to 100m in topographic elevation is evident across the "flat" part of the DEM
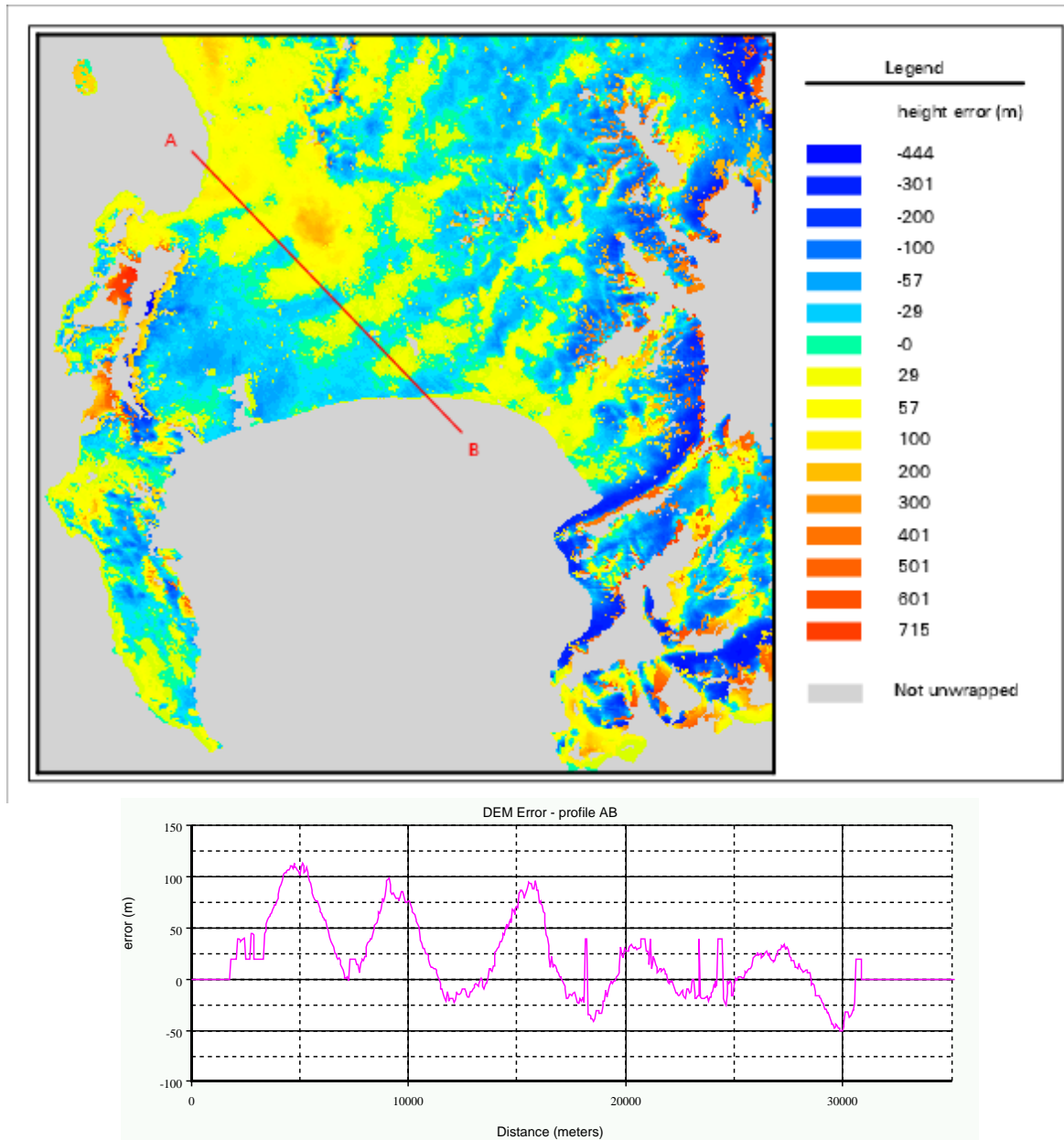
Figure 3.3: Elevation error map and profile

(Figure 3.3 and Figure 3.7). It has not been possible to verify the weather conditions at the time of data acquisition, but the periodicity, orientation and dimensions of this feature would seem to suggest that it is almost certainly due to a set of cirrus clouds present during acquisition of one of the images. A further phase delay artifact (Figure 3.8) appears as a hole or depression just to the north west of Cape Town international airport. This apparent depression is roughly 4km in diameter and equivalent to 200m deep! It is possible that this artifact might be due to the effects of a grass fire just north (down wind) of the runway. The smoke from such a fire would contain significant amounts of moisture, and could be the cause of significant phase delay of the incident radar signal. The changes in local atmospheric refractive index that the exhaust from a large aircraft might have, could also be speculated on. The shape of the aberration would seem to imply some sort of point source, the effects of which have been dispersed downwind. The presence of this "fire" or aircraft exhaust plume is again mere speculation, as its occurrence has not been verified. The location of wind shadow on the sea (Figure 3.9), the sea surface waves, the direction of the inferred cirrus clouds (Figure 3.7), and the shape of the phase aberration just to the north west of Cape Town international airport (Figure 3.8), all correspond with a south-easterly wind (a particularly common weather state for Cape Town).

Another error that is quite noticeable, is a linear trend across the DEM. This trend, which is very similar to that seen in the Katse study (Chapter 4), effectively gives the DEM a tilt to the north, placing the northern region approximately 100m lower than it should be. This error is likely to be due to an error in the baseline estimation, which could in turn be due to inaccurate ground control information. Correcting this error should in theory be fairly simple, but in the presence of the atmospheric effects, perhaps not so. In general, a much larger corpus of ground control points can be utilised, carefully selected to be in flat regions where posting errors will not be significant.

3.6 Conclusions and recommendations - Cape DEM

In spite of the high coherence between the images and the favorable viewing geometry, the height map generated contains significant artifacts and inaccuracies. Whilst this is of concern for the viability of repeat pass interferometry for DEM construction, it is serendipitous in that it has provided us with an invaluable opportunity to study the practical limitations of the technique, and in particular, the effects of atmospheric inhomogeneities on InSAR. On the other hand, the presence and magnitude of the artifacts in the DEM are a grave concern in the use of this technique for deformation studies. If we can anticipate anomalies of this nature in repeat pass interferometric products, we have to be extremely careful in our interpretation of differential fringe patterns produced by dInSAR.

In the production of DEMs, the errors and aberrations can in theory be overcome, or at least minimized. The time delay due to atmospheric effects is independent of frequency [6]. It is therefore not possible, as with GPS and radar altimeter surveys, to correct the error using multi-frequency systems, but they can be overcome by using a dual antenna system. With repeat pass systems, the errors can be minimized by averaging the phase contributions from numerous passes, and by the inclusion of comprehensive ground control data.

The "holes" in the data, caused by discontinuities in phase unwrapping can be overcome by a number of means: If the scene is viewed interferometrically from more than one direction, it is quite likely that different regions will unwrap in the different interferograms. These could then be combined in an appropriate way so as to fill the gaps. A sensor with a larger incidence angle would be advantageous under these circumstances. Any gaps that remain after this approach could be interpolated or filled using data acquired by other means. This is the approach used in the Shuttle Radar Topographic Mapper (SRTM) mission, a dual antenna, fixed baseline, system. It is also possible that an alternative approach to phase unwrapping, such as the minimum cost flow algorithm might prove more robust. A number of unwrapping methods could possibly be combined or averaged to produce a more complete and accurate data set.

The errors in the phase to height calculations done in this study should be reduced by improving on the ground control. The ground control points should be carefully selected, not only so that their positions and elevations are accurate, but also so that they fall within regions of high coherence.

It is apparent from this study and from the literature, that the production of precision DEMs is likely to remain a multidisciplinary subject. Whilst InSAR is capable of producing high resolution height
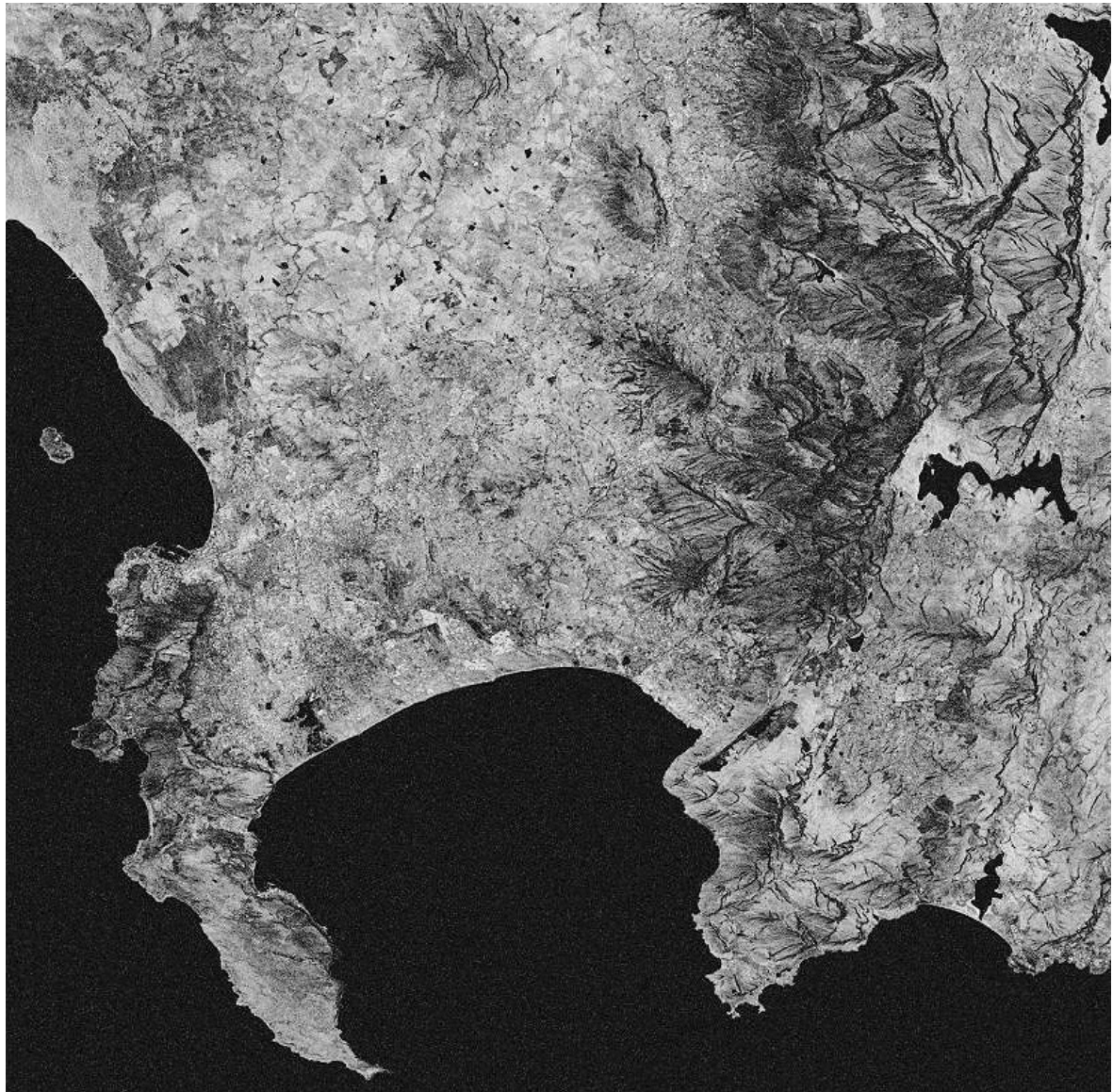
Figure 3.4: Phase coherence map for Cape Town interferometric image pair
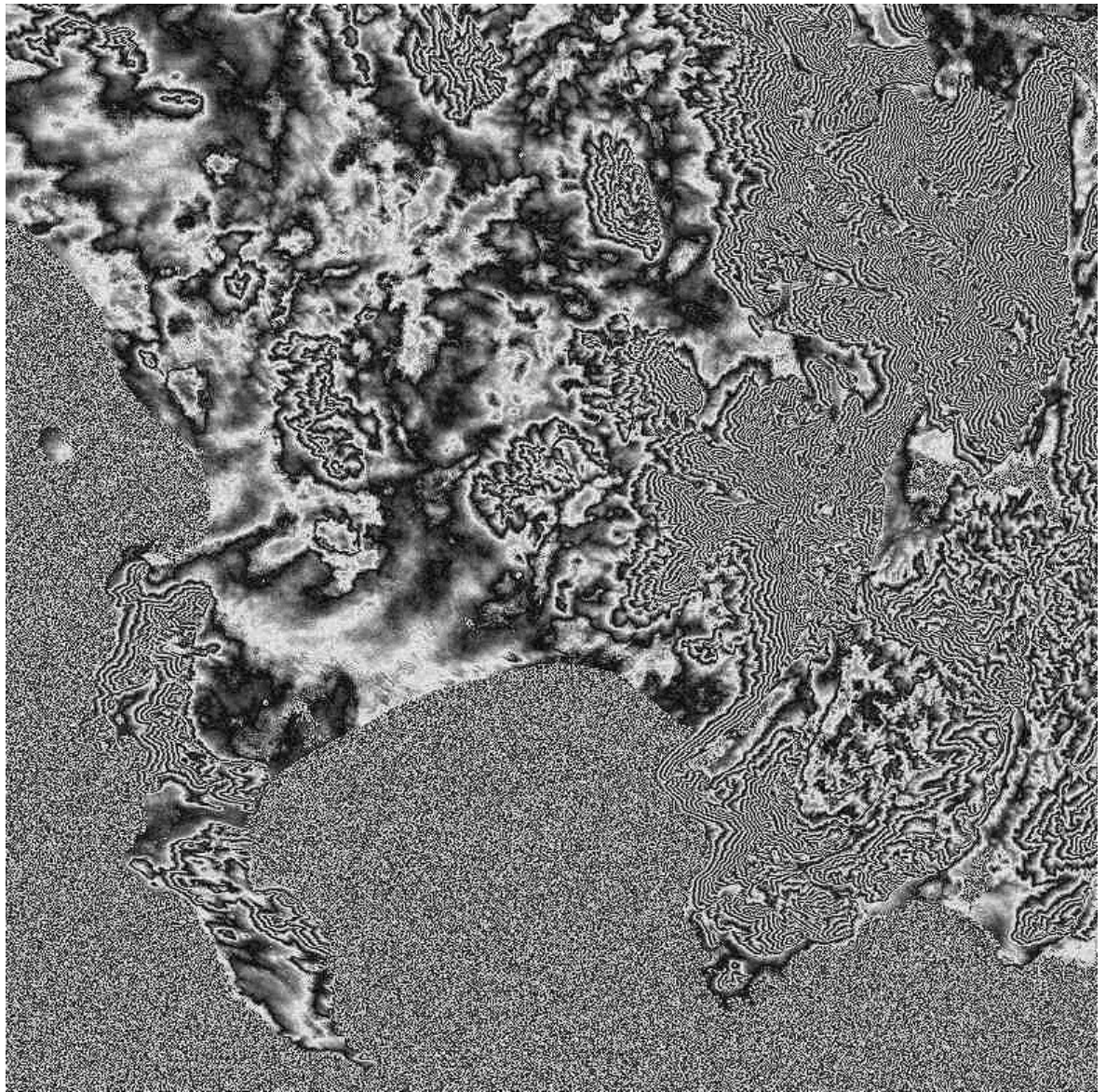
Figure 3.5: Flattened phase, 05715_25388
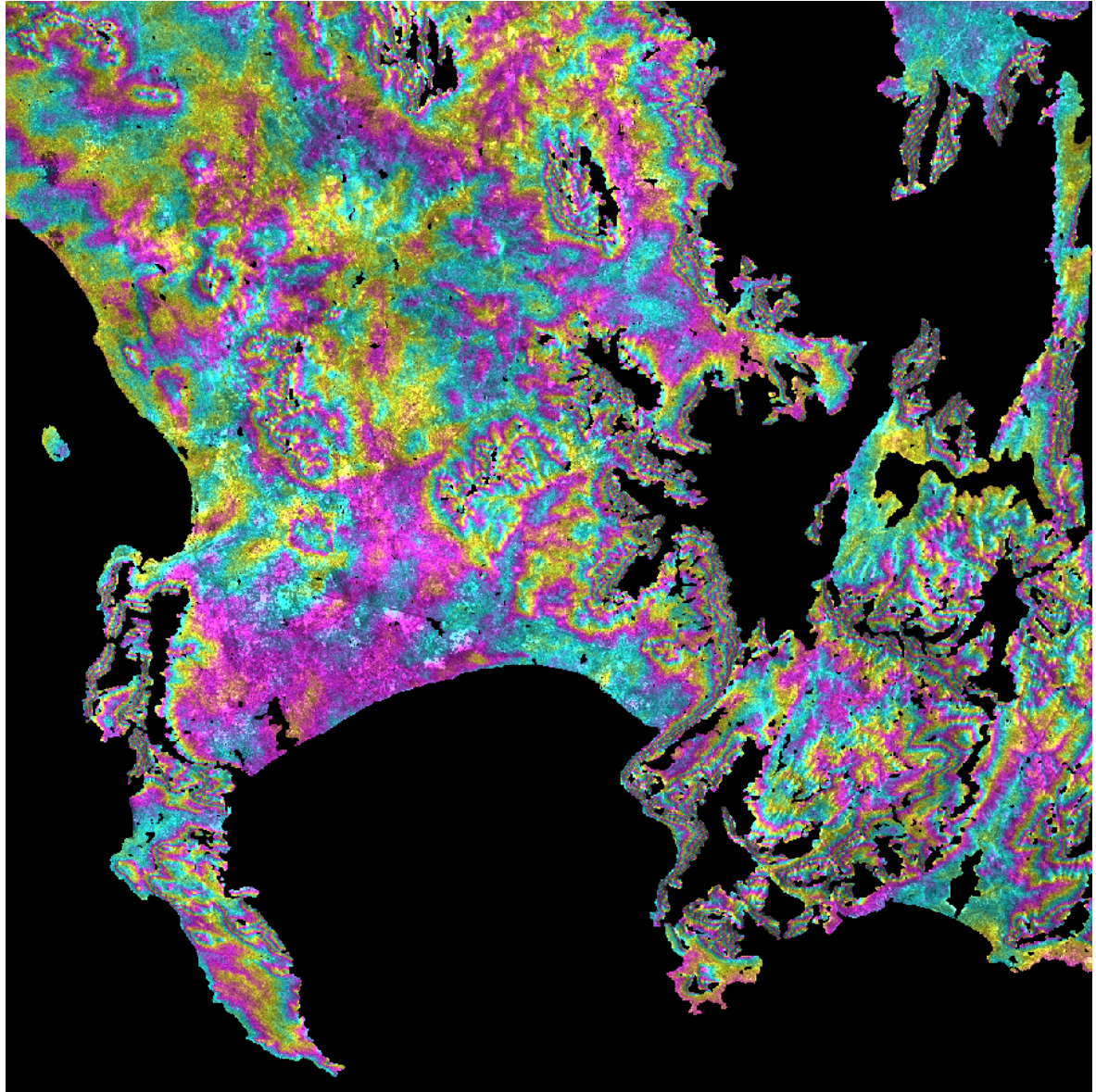
Figure 3.6: Flattened phase with regions that would not unwrap masked
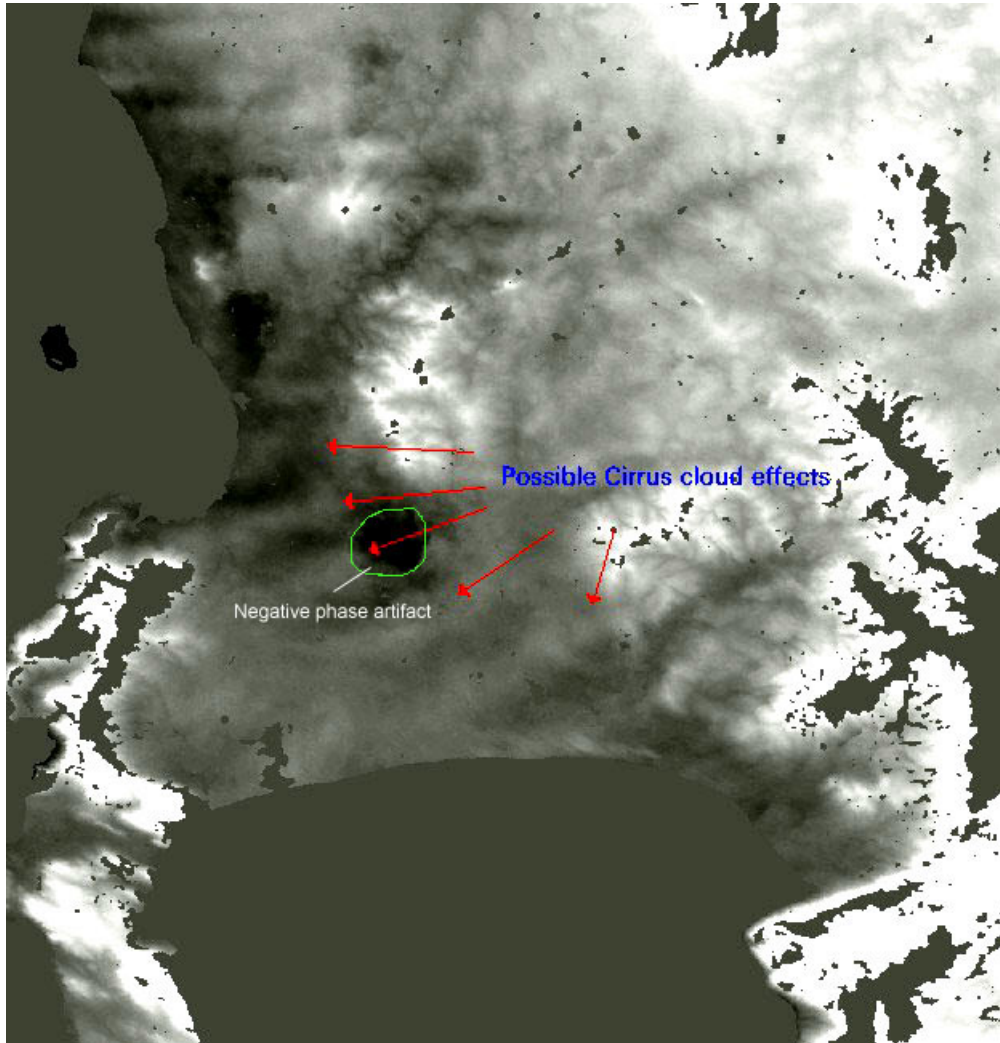
Figure 3.7: Grey scale height map. Artifacts indicated
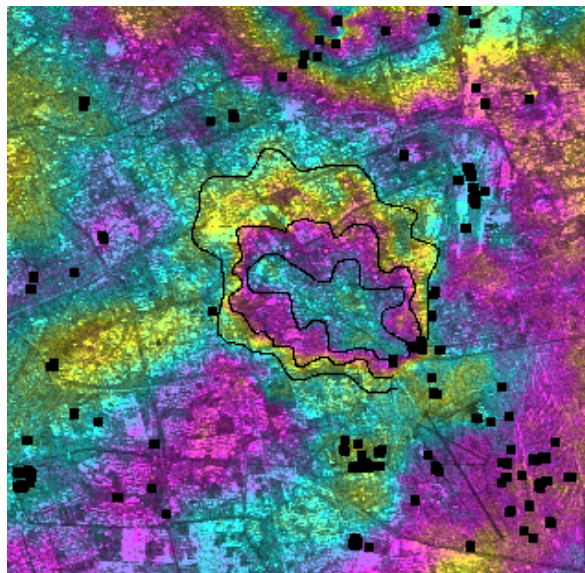
Figure 3.8: A significant atmospheric artifact NW of the airport

maps, the control and external input is such that it makes good sense not to ignore other technologies. The acquisition of almost complete global coverage of dual antenna InSAR data in c-band and x-band, was accomplished in February 2000 during the SRTM mission [8]. Whilst it is going to take at least two years to process the nearly 15 terabytes of raw data, the final products should represent the highest quality DEMs available.
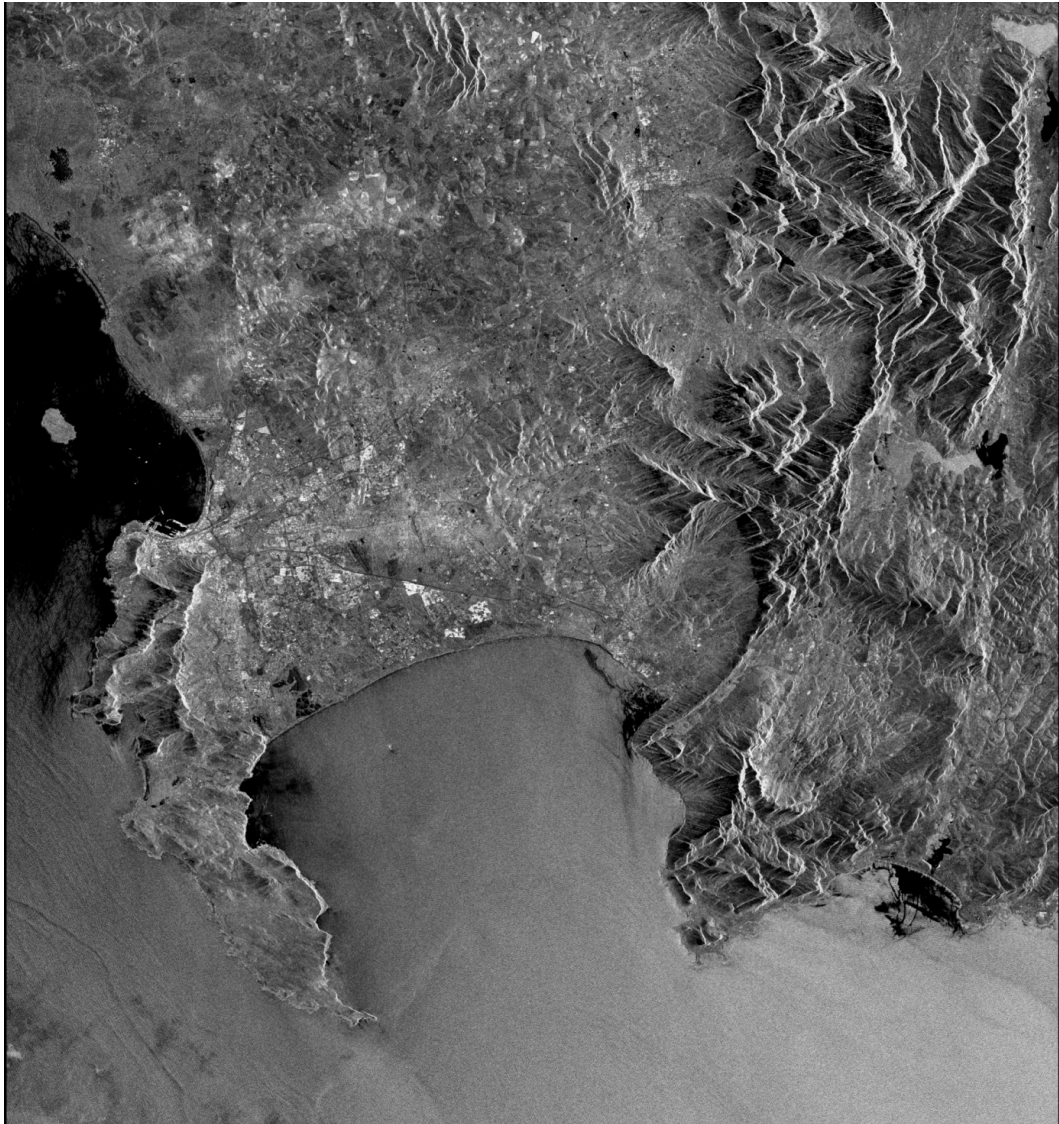
Figure 3.9: ERS multi-look intensity image of study area

Chapter 4

Katse Loading Experiment

4.1 Introduction

This study was concerned with the mapping by differential interferometric synthetic aperture radar (dInSAR) of the loading effects of the Katse reservoir on the Earth's crust. This is a complex experiment, which, like the Welkom earthquake experiment (Chapter 5), involved the use of satellite borne radar in the detection and mapping of very small ground deformations over large areas. The results of this study were to be used to gain a better understanding of the rheological and structural nature of the Earth's crust in the region, and to improve our ability to assess the seismic risk involved in building large reservoirs in the Lesotho Highlands (Figure 4.1).

Figure 4.1: Map showing the location of the Katse Reservoir and the ERS data used in this investigation

4.1.1 Project Overview

When a large dam or reservoir is constructed, the loading effect of the impounded water changes the local stress regime in the Earth's crust. This loading is often sufficient to cause flexure of the

Earth's crust in the order of tens of centimetres [9]. Furthermore, the altered stress conditions, and the increased fluid pressures in the pores and fractures of the rock strata are often sufficient to trigger earthquakes through brittle failure and remobilization of existing rock fractures (reservoir induced seismicity). In some cases, such as that of the 1969 Koyna disaster in India [9], this phenomenon has had devastating effects on local populations.

The amount and type of seismicity induced by a reservoir is related to, among other things, the thickness and elastic properties of the Earth's crust in the vicinity of the reservoir. As it is not possible by conventional means to accurately model these rheological properties of the Earth's crust to a significant depth, many assumptions have to be made with regard to factors such as its flexural thickness. These assumptions are then used to model and predict the effects of reservoir loading.

The usual methods used for monitoring crustal deformation associated with a new reservoir involve using a benchmark network and conventional geodetic techniques. These techniques are reliable, and as such, cannot be replaced. They do however require on-site repeat measurements to be made by land surveyors, and furthermore, these measurements can only be obtained in a discrete and limited number of positions. Recent studies in Differential Interferometric Synthetic Aperture Radar (InSAR) have shown it to be a potentially useful tool for precise measurement of small (1 cm or less) ground deformations with good resolution (10 m) over large areas (100 km swaths) [3].

On the basis of successful work by other groups doing research into InSAR studies of phenomena such as co-seismic displacement (ground deformations associated with Earthquakes) and ground subsidence resulting from sub-surface mining activities [5] [10] [11] [12], it was proposed in 1996 that, using SAR data acquired before and after the filling of the Katse Reservoir, it might be possible to map the deformation caused by added mass of water. If a plausible result were forthcoming, it would then be feasible to draw inference with regard to the unknown geophysical parameters relating to the crust.

4.2   Site selection

The Katse Dam (Figure 4.2), which represents the keystone in the Lesotho Highlands Water Project, is the highest (185m) dam in Africa, and one of the highest of its type in the word. It is situated on the Malibamatso and Bokong rivers (headwaters of the Orange River), and it impounds approximately two billion tonnes of water in a lake more than 20 km in length [13].

Figure 4.2: Katse Dam - Keystone of the Lesotho Highlands Water Project

The commencement of filling in October 1995 of the Katse Reservoir, and the subsequent rapid rise in water level happened by chance to coincide with the first ERS Tandem mission, a special phase of interferometric data collection by the European Space Agency's two imaging radar satellites, ERS-1 and ERS- 2. This Tandem mission provided us with almost ideal preloading InSAR data sets, and consequently also with a unique opportunity to use this technique to study the response to an imposed load of the Earth's crust in the Lesotho region. The loading effect of the Katse reservoir was of particular interest, as there had been some speculation as to the actual tectonic setting of the Lesotho Highlands Water Scheme. One of the fundamental uncertainties being the flexural thickness

of the Earth's crust in this region, and how this would affect the amount of deformation and seismicity that would take place.

Early predictions based on an elastic half-space model [14] indicated that the load of the Katse Reservoir should have induced a maximum vertical displacement of the crust in the order of 10-20 cm, centred at a point about 5 km upstream of the dam wall. The lateral extent of the deformation was expected to extend beyond 50km from the reservoir, at which distance the modeled vertical displacement would be in the order of 1mm. For the purposes of SAR interferometry, this distal effect would be outside the noise limit of the technique, and so could be regarded as the effective edge, or half-width of the anticipated deformation. For the purposes of the preliminary studies and risk assessment for the construction of the Katse reservoir, it was assumed, based on entrenched ideas, that the Lesotho highlands represent a region of thick, stable crust. Recent research [15] indicated however, that this region may in fact be part of an incipient plate boundary, forming the southern extension of the East African Rift system. This hypothesis was considered when a value for crustal thickness was selected for the elastic half-space model.

4.3 Geology

4.3.1 Stratigraphy

The Katse reservoir is located in valleys of the Malibamatso and Bokong rivers in northern Lesotho. These valleys are deeply incised into the Jurassic age Drakensberg flood basalts, which represent an erosional remnant of a violent episode of volcanism associated mainly with Gondwana breakup. The main episode of volcanism having occurred between 200 and 190Ma [16]. The ~140 000 km^2 Drakensberg plateau is the largest remnant of a sequence of lavas which are believed to have covered much of southern Africa. The preserved thickness in the Drakensberg is 1400m (The Lebombo belt to the north of the Drakensberg is characterised by over 10km of volcanic succession).

The volcanic succession is under lain by a thick sequence of Permo-Triassic sediments, which in turn, lie unconformably on the gneissic basement rocks of the Archaean age Kaapvaal and Pan-African age Namaqua-Natal tectonic provinces.

Lesotho is host to a number of late Cretaceous age Kimberlites, some of which are diamondiferous. The presence of these Kimberlites is possibly significant to the question of crustal thickness, in that a requirement for these diatremes to be diamondiferous is that they originate from a depth of around 250 km.

4.3.2 Geological structures and geophysics

The entire Lesotho region is characterised by a pervasive NW-SE trending fault and joint system, which includes numerous syn or post tectonic dolerite intrusions. These dykes and sills, the ages of which correspond with that of the flood basalts, are the hyperbyssal expression of the basalt out-pourings.

The Bouger gravity map of Lesotho (Figure 4.3) shows a significant positive anomaly (the Thaba Tseka anomaly) in the middle of Lesotho. There are three possible reasons for this anomaly: The one possibility, which has been proposed by Hartnady [17], is that this is a region of crustal thinning, and uplift. This hypothesis is supported not only by the anomalously high gravity field, but also by seismic activity and an abnormally high geothermal gradient. This has been called the Quathlamba hot-spot hypothesis, which implies that the gravity anomaly is due to a state of isostatic disequilibrium, in which the Drakensberg mountains are "higher than they should be". The other possibility is that the composition of the crust in this region has an anomalously high mafic content. Although it is difficult to account for the full gravitational effect, this would seem reasonable considering the volume of doleritic and basaltic material present. There is significant evidence to suggest that the crustal thinning hypothesis is quite plausible [15], and it is hoped that the results of this study should serve either to prove or disprove this theory.
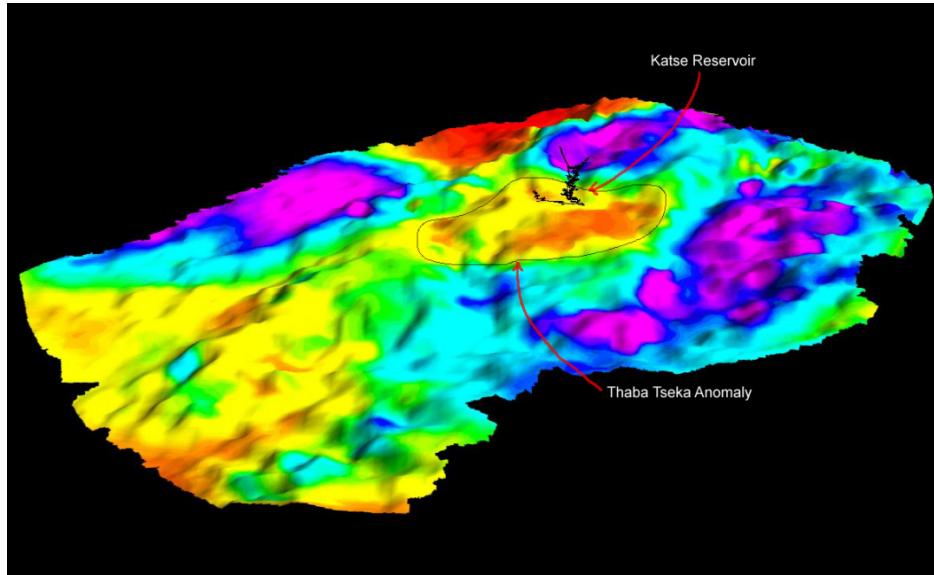
Figure 4.3: Bouger gravity of Lesotho overlaid on elevation

4.3.3 Seismicity and plate tectonics

Another major motivation behind this investigation was that of concern raised by Hartnady, and others, about the tectonic setting of the Lesotho Highlands Water Scheme [17][15]. Subsequent to the original impact assessment and dam design phase in 1988-1999, new evidence accrued [18] to refute the previously entrenched idea that the Lesotho region lies within a tectonically stable, "intra-plate" area. The accretionary boundary, or suture zone between the Kaapvaal Craton and the Namaqua-Natal tectonic province, as inferred by interpolation and gravity mapping, coincides roughly with the NE-SW trending Drakensberg mountains. Furthermore, a seismically active belt trending roughly East-West across the southern Drakensberg between Kwazulu Natal and the Southern Freestate is evidence of "an embryonic extension of the East African Rift system" [15]. Hartnady states that "the recent seismic activity (Richter magnitude 5 event on 5 October 1986) in the Transkei-Lesotho border region is related either to southward propagation of the East African Rift System, or to epeirogenic causes involving the (postulated) sublithospheric Quathlamba hot-spot". Either of these hypotheses would involve a reduction in both the flexural thickness, and the competence of the lithosphere. The seismic history of Southeast Africa provides strong evidence to support a hypothesis originally proposed by Alex L. du Toit in 1933 [19], in which he proposed a southern extension of the East African Rift System, with the boundary between the Somalian and Nubian plates extending southward through the Lesotho region. The position of the Euler pole of rotation for these two plates is inconclusive, but current consensus, which lends further support to the rifting hypothesis, places it somewhere in the far Southern Ocean.

4.3.4 Crustal loading and flexure

In order to assess the likelihood of seismic activity associated with the filling of a reservoir, and to predict the magnitude and consequences of such events, a comprehensive geological and geophysical investigation of the proposed site is necessary. Such a study, which is mandatory in the case of large dams[1], includes the modeling (prior to construction) of the loading effects that the new water mass will have on the Earth's crust, and subsequent monitoring of the real deformation during and after impoundment. The physical parameters used in deriving the model include certain rock characteristics and the flexural thickness, making up the flexural rigidity of the Earth's crust in the region concerned. It is this flexural rigidity that is the main factor affecting the amount of deformation that will take place [20]. In order to determine the flexural rigidity of the crust, a value for the crustal thickness is

---

[1]A large dam is deemed by the International Commission on Large Dams (ICOLD) to be one exceeding 100m in height, and storing more than $1km^3$ of water

required, and it is this parameter that is likely to be the least well defined. The value used is generally based on a combination of gravity measurements, seismic velocities and regional tectonic postulates.

4.3.5 Crustal loading and flexural rigidity

The Earth's continental crust represents a thin (10 to 50 km) [20], partially flexible layer floating on the more dense, but ductile asthenosphere. When a load is either imposed on or removed from the surface of the Earth, the crust responds in a manner very similar to that of an elastic sheet floating on a viscose liquid. For example, the vertical displacement z of the oceanic lithosphere under loading can be calculated by modeling it as an elastic sheet by solving the fourth order differential equation 4.1:

$$D\frac{d^4z}{dx^4} + (\rho_m - \rho_w)zg = P(x) \tag{4.1}$$

where $P(x)$ is the load as a function of horizontal distance x, g the acceleration due to gravity and ρ_m, ρ_w the densities of asthenosphere and sea water respectively. D is a parameter termed the flexural rigidity, which is defined by equation 4.2:

$$D = ET^3/12(1 - \sigma^2) \tag{4.2}$$

where E is Young's modulus, σ Poisson's ratio and T the thickness of the lithosphere.
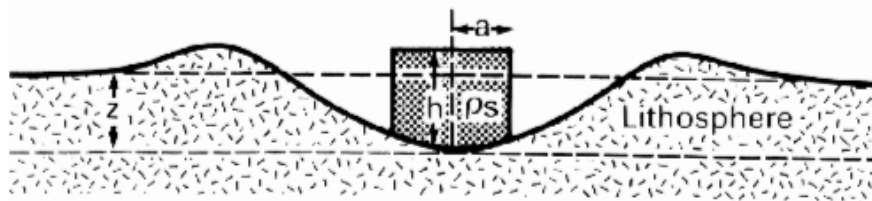
Figure 4.4: Flexure of the lithosphere as a result of a two dimensional load

The relationship between the maximum displacement z and the load for a two-dimensional load of half-width a, height h and density ρ_s shown in Figure 4.4 is:

$$z_{max} = h(\rho_s - \rho_w)(1 - e^{-\lambda a}\cos\lambda a)(\rho_m - \rho_s) \tag{4.3}$$

where

$$\lambda = ^4\sqrt{(\rho_m - \rho_w)\,g/4D} \tag{4.4}$$

It can be shown that while loads with half-widths in excess of about 500 km are in approximate isostatic equilibrium, loads with a half-width of less than about 50 km are supported by the finite strength of the lithosphere [20]. This, in part, accounts for the phenomenon of reservoir induced seismicity, which results from brittle failure in the crust.

4.4 Materials and Methods

4.4.1 ERS data

Many of the procedures used in differential interferometric processing[2] are common to those used in the production of digital elevation models by interferometric SAR. As these have been discussed in chapter 3, only issues relating specifically to the processing of Katse data will be presented here.

---

[2]All SAR processing was done using the WRC funded Gamma suite of processors.

Data Acquisition

In late 1995 and early 1996, Tandem ERS images were acquired over the Lesotho region. Because of the short period (1 day) between repeat passes, and the close similarity in the respective orbit paths, the data from this Tandem Mission is particularly well suited to interferometric work. If the topography of the area was not such as to cause undue problems with phase unwrapping, these data sets would have been the best available for the generation of a DEM of the area. Such a DEM would have been used for removal of the topographic component of differential interferograms.

Six Tandem image pairs were acquired over the Katse region between December 1995 and April 1996 (Table 4.1). However, for technical and scheduling reasons, there was a two-year hiatus in image acquisition by ERS satellites over Lesotho. After consultation with the European Space agency, and by arranging a co-operative understanding with a UK based research group and the British Council for Sciences, we managed to secure a further 60 potential data takes.

Table 4.1: Data selection table for Katse InSAR project - Tandem pairs have 1 day temporal separation.

ERS data for Katse project Track 443 Frame 6597

B perp values taken from: http://earthnet.esrin.esa.it/pub/baseline/baseline.html

Delta - days

			E1-22976		E2-3303		E1-23477		E2-3804		E1-24980		E2-5307		E2-20838		E2-21339	E2-21840
E1	06-Dec-95	22976	0															
E2	07-Dec-95	3303	1	-160	0													
E1	10-Jan-96	23477	35	-89	34	71	0											
E2	11-Jan-96	3804	36	-211	35	-51	1	-122	0									
E1	24-Apr-96	24980	140	669	139	829	105	758	104	880	0							
E2	25-Apr-96	5307	141	577	140	737	106	666	105	788	1	-92	0					
E2	15-Apr-99	20838	1226	556	1225	716	1191	645	1190	767	1086	-113	1085	-21	0			
E2	20-May-99	21339	1261		1260		1226		1225		1121		1120		35		0	
E2	24-Jun-99	21840	1296	57	1295	217	1261	146	1260	268	1156	-612	1155	-520	70	-499	35	0

A further seven images were acquired after September 1998, but the only image pair that spans the filling of the reservoir, and which offers a sufficiently small baseline to ensure reasonable phase coherence over the time period, is the pair 24980_20838 of April 1996 and April 1999 respectively. 35 day repeat acquisitions by ERS-2 will continue until the end of the current ERS imaging phase (December 2000).

Fortuitously, the ERS tracks over Lesotho are such that the Katse Reservoir is located near the edge of the scene (Figure 4.1). The reason that this is preferable to having the load in the centre of the image is that, although one would not see the full deformation picture, or any broad-scale asymmetry in the deformation, one would at least be maximising the lateral extent to which the deformation could be mapped. Without being able to image the full lateral extent of the deformation, it would not be possible to count all the deformation fringes, and hence it would not be possible to calculate the vertical extent of the deformation either.

4.4.2 Processing

The processing methods used on the Katse ERS data were essentially the same as those used on the Cape data, except that this was a differential problem, thus requiring processing beyond the extraction of height information. The processing details are presented in appendix C.

The problem of topographic phase removal

Phase unwrapping is probably the most difficult aspect of InSAR processing, and is also susceptible to errors. If possible, in dInSAR, phase unwrapping should be avoided. Due to the nature of the topography around the Katse reservoir, it was not possible to completely unwrap the phase of any of the Tandem interferograms. As a result, it was necessary to make use of an independently derived DEM for the removal of the topographic phase component from the interferograms. Use was made of a DEM which was derived by combining a DEM generated by means of stereo reduction of overlapping SAR images with one digitising from topographic maps.

4.5 Stereo ERS DEM production

As with aerial photography, parallax differences in overlapping SAR images can be used to derive a terrain height information. Two images of the same scene, but acquired from different viewing angles, are required. They are compared quantitatively for differences in distortions which are caused by the foreshortening effect of topography in SAR images. Foreshortening is the term given to the apparent shift towards the "near-range" side of the SAR image of high points on the ground. The amount by which a topographic feature is foreshortened is proportional to the height of the feature, and inversely proportional to the radar incidence angle. The height of the feature can therefore be determined from the magnitude of the foreshortening and the viewing geometry.

A pair of ERS-1 images (E-1 15523 and E-1 16585) from different acquisition phases was used for the stereographic generation of a DEM of the Katse region. These images have an approximately 60% overlap, giving them a viewing angle difference of approximately 2.5° (both scenes ascending orbit, right looking). For stereo work, this is a very small difference in viewing geometry, and is far from ideal, but there was no harm in trying! The software used was the ERDAS StereoSAR beta release.

4.5.1 Procedure

After selecting an image pair, the procedure followed is outlined below.

Input The two images were input as Reference and Match images. For the initial geometry calculations, the state vectors are read from the image header. This flight path information can be improved by entering some well distributed ground control point.

De-speckle The images were both filtered with a Gamma-MAP filter for reduction of speckle.

Registration The image registration process uses an intensity auto-correlation sequence with a tunable hierarchical pyramid to define match points. The first step involves an affine transformation and re-sampling of the Match image so that its geometry corresponds with that of the Reference image. The registration process benefits from the definition of tie points, which should be well distributed around the scene in the lowest and the highest regions. In Lesotho, individual huts with steel roofs make excellent single pixel tie points. The correlation process, which can be evaluated for effectiveness by inspection of a correlation image, then performs the final image registration.

DEM generation This next step involves a pixel by pixel calculation of parallax and conversion to a height map.

4.5.2 Result and post processing

The stereo DEM produced was significantly degraded by noise, the source of which, was probably a random registration mismatch due to residual speckle. This noise could be reduced at the expense of resolution.

When an attempted was made to improve the flight path information using corner co-ordinates provided in the image headers, the resultant DEM developed a ramp to one side of approximately 10° (Figure 4.5).

When processed without ground control, that is to say, using only the ephemeris data from the original CEOS headers, the result was much improved, in that the DEM no longer suffered from the tilt to the east. However, there was a significant error in the absolute height values, with the peaks appearing higher than they should have, and the valleys lower. This was assumed to be the result from the sensitivity of this technique to errors in the measured radar slant range, the main limiting factor in radargrammetry[21] (equation 4.5). This error was reduced by applying a scaling factor, but a significant low frequency error remained due to some non-linearity in the error. In spite of this however, there remained useful high frequency information in the DEM (Figure 4.6).
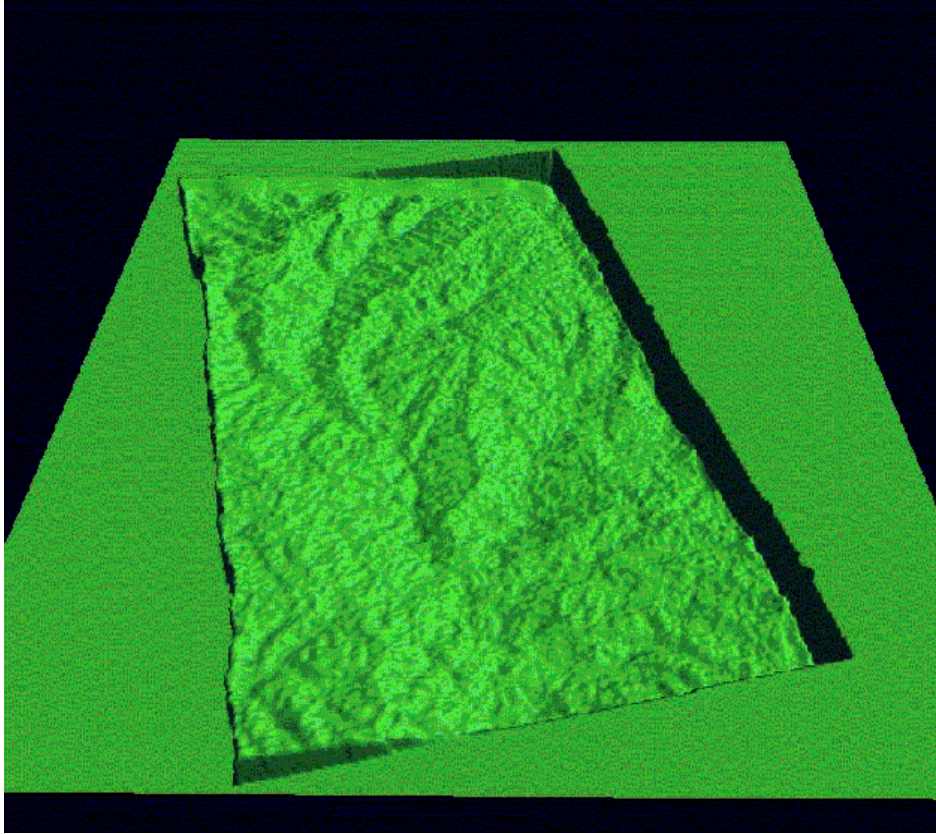
Figure 4.5: Stereo ERS DEM - generated using "corrected" flight path (corner co-ordinates and altitudes derived from SAR processor output). A regional error has been introduced, resulting in a tilt to the east (away from the sensors).
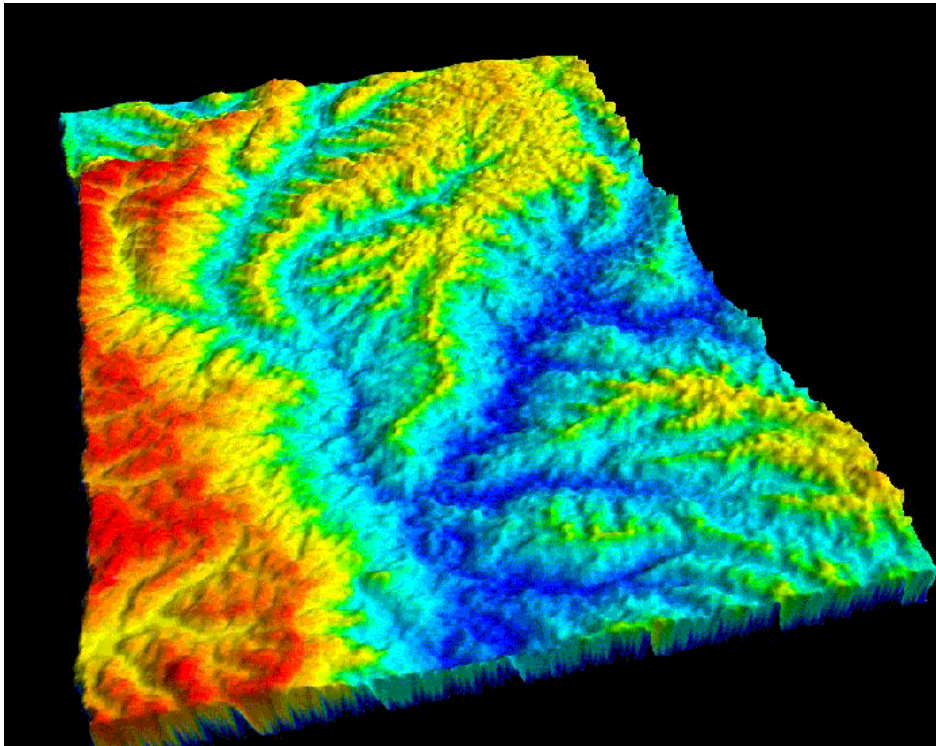
Figure 4.6: Stereo SAR DEM - "corrected" - generated using coarse ephemeris data alone (without ground control).

A low resolution (1 minute postings) DEM, derived by digitising points from topographic maps, provided the reasonably accurate low frequency information that the stereo DEM lacked. This DEM was interpolated to the same resolution as the stereo DEM (2 km to 50 m) by resampling and low pass filtering. The high frequency component of the stereo DEM was was then added to it to produce a merged product. This final product, although by no means accurate, was sufficiently detailed for the simulation of SAR products, for use in topographic phase removal in differential InSAR (section 2.2.8).

In order to provide a DEM that covered at least the area of the images being used for InSAR processing, the stereo DEM had to be feathered into the coarse DEM (Figure 4.7), which covered the whole of Lesotho.
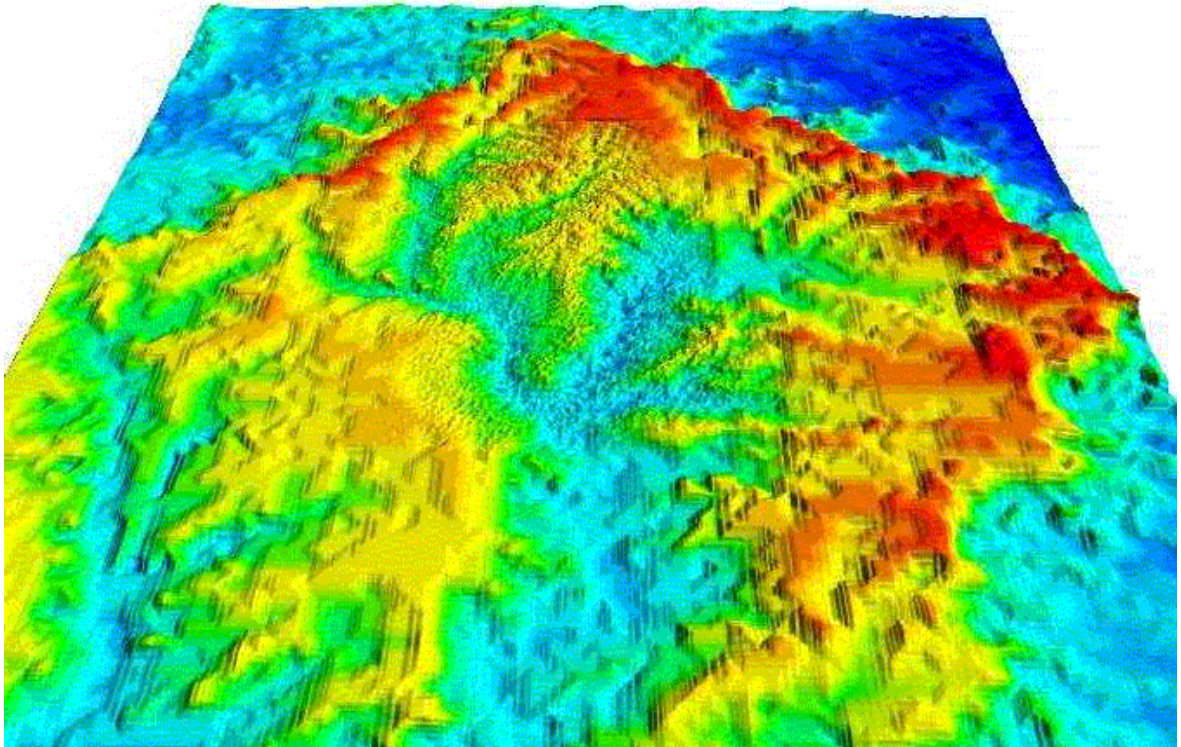
Figure 4.7: Stereo DEM inserted into coarse DEM

4.5.3 A comment on image selection for stereo SAR

For stereo processing, the image selection process is one of compromises, and there are several important factors that should be considered. The two overlapping images must be selected so as to maximise the intersection angle in the viewing geometry, but not so much that the images cannot be registered. The optimum geometry depends primarily on the amount of relief in the scene. Areas with very little relief are best imaged from opposite sides, whilst those with high relief require a much smaller intersection angle.

The error in the terrain height estimate σ_h due to the error in slant range measurement σ_r is [21]:

$$\sigma_h^2 = \left\{ \frac{(\sin^2 \theta' - \sin^2 \theta'')}{\sin^2 (\theta' - \theta'')} \right\} \cdot \sigma_r^2 \qquad (4.5)$$

It will also be noted from this equation that when the difference between the two look angles, θ' and θ'', is small, the technique becomes very sensitive to errors in the viewing geometry. For this reason, ERS image pairs from the same orbital direction, in which the difference in look angle can be no more

than 3 or 4 degrees in the overlapping section, are not really appropriate for stereo DEM construction. With a 60% overlap, the difference in look angle is less than 3 degrees. Ideally, a sensor like Radarsat, which employs beam steering should be used to obtain a reasonable variation in the look angles.

The availability of data was the limiting factor in this study, as the cost of requisitioning Radarsat data takes would have been prohibitive. ERS data was the only data available to us, but in retrospect, it may have been more appropriate to use a pair of crossed track images.

4.5.4 Alternative height mapping methods

Of course, there are many other methods that could be used for the generation of height maps. These range from scanning airborne Lidar to stereo optical photogrammetry. Cost was the fundamental reason why none of these techniques were employed. Even the photogrammetry would have been too costly because of the software requirements.

4.6 Removal of topographic phase component in differential interferometry

The actual process of topographic phase removal using an independent DEM involves careful registration of the DEM with the interferogram (produced from image pair 24980_20838), with subsequent simulation of interferometric phase. The simulated interferogram is then subtracted from the real one, and in theory, only the differential component of the phase should remain (with residual topography due to DEM errors - refer "Independent DEM requirements" in Chapter 2.1).

4.7 Experimental control

For control purposes, survey data (Table 4.2) from monuments near the wall of the Katse Dam (Figure 4.8) was made available by the Department of Water Affairs Table. The pertinent information in the table is that of the reference beacon displacements. The maximum displacement is less than 2 cm.
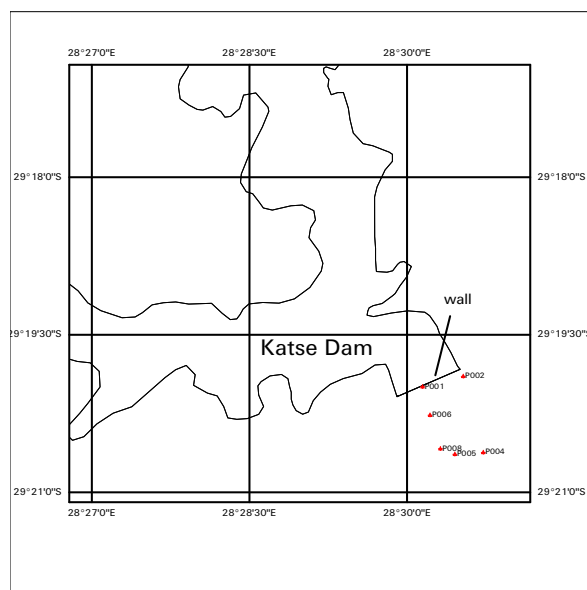
Figure 4.8: Map indicating survey monument locations

Table 4.2: Survey monument deflection monitoring
KATSE monument deflections

LIST OF MEASUREMENTS:

MEASUREMENT	DATE	WATER LEVEL
9101	1991.01.09	
9211	1992.11.25	
9612	1996.12.04	2016.88
9702	1997.02.02	2027.83
9703	1997.03.10	2030.96
9803	1998.03.02	2051.69
9807	1998.07.22	2049.51
9902	1999.02.27	2051.03
9908	1999.08.25	2044.44

LIST OF CO-ORDINATES AND HEIGHTS:

Reference measurement: 9101

BEACON	Y	X	Z	REMARKS
	LO 29			
P001	48325.535	3246048.722	2075.8770	PILLAR
P002	47699.236	3245863.306	2097.3744	PILLAR
P004	47384.706	3247200.934	2118.8168	PILLAR
P005	47822.661	3247234.530	2130.2514	PILLAR
P006	48045.664	3247138.180	2131.2325	PILLAR
P008	48208.489	3246548.448	2099.7160	PILLAR

DISPLACEMENTS - REFERENCE MEASUREMENT: 9101

BEACON	P01	P02	P04	P05	P06	P08
MEASUREMENT	dz in mm	dz in mm	dz in mm	dz in mm	dz in mm	dz in mm
9211	0.4	0.2	-0.4	0.0	-1.6	-1.7
9612	-11.6	-8.7	0.0	-2.6	-0.5	-11.1
9702	-12.5	-12.4	0.0	-1.9	-2.4	-11.1
9703	-11.6	-11.1	0.0	-0.9	-3.3	-13.3
9803	-14.7	-18.7	0.2	-0.4	-3.7	-14.2
9807	-15.0	-18.6	0.0	-4.0	-4.4	-15.3
9902	-17.7	-17.3	-0.1	-1.5	-0.7	-12.7
9908	-13.4	-16.6	1.9	-0.8	-1.5	-12.1

4.7.1 Reservoir Levels

For purposes of load calculation, reservoir water levels were obtained from the Department of Water Affairs (Figure 4.9). These data are based on the usable supply, or minimum operating level of the reservoir, and do not include the initial rapid filling phase between October 1995 and March 1996.
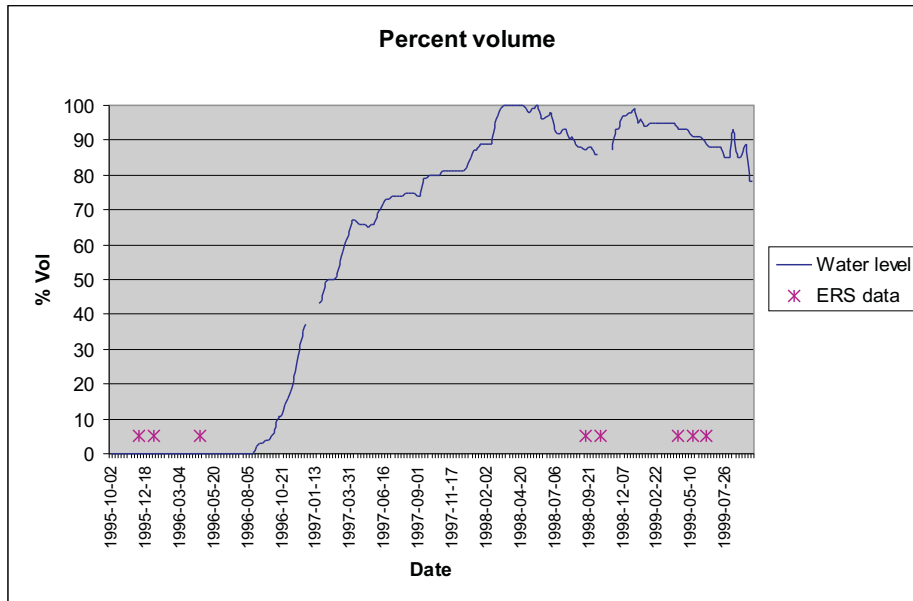
Figure 4.9: Katse Reservoir water levels

4.8 Results and discussion

Chronology of events

October 1995	Katse impoundment (commencement of filling)
6/7 December '95	First ERS Tandem pair acquired over Katse area
Dec. 95 - Jan. '96	Heavy rain, rapid initial inflow to Katse.
3 January '96	Ha Mapeleng seismic event (1.5 km by 7 cm crack appears in Katse basin) Ref. "News", Nature vol 380, 21 March 1996
10/11 January '96	Second ERS Tandem pair acquired over Katse
April 1996	Katse reaches 45% by depth (approx 20% by volume)
24/25 April '96	Third ERS Tandem pair acquired over Katse
December '97	Construction of Katse Dam completed (85% full by volume)
March '98	Katse overflows
Late '98	Construction starts on Mohale Dam
17 September '98	ERS-2 data take (baseline excessive) (ERS-1 no longer serviceable)
22 October '98	ERS-2 data take (baseline excessive)
January '99	ERS-2 orbit adjustment secured for Katse project.
15 April '99	ERS-2 data acquisition over Katse (and every 35 days thereafter).

Tandem ERS image pairs from the 1995, 1996 mission were processed early in the course of this project by Eric Rignot at JPL in California. The outcome of this processing represented strong support for the viability of the interferometric technique for this project. The interferograms that were produced indicated good coherence even in regions of fairly extreme radar foreshortening (Figure 4.10).
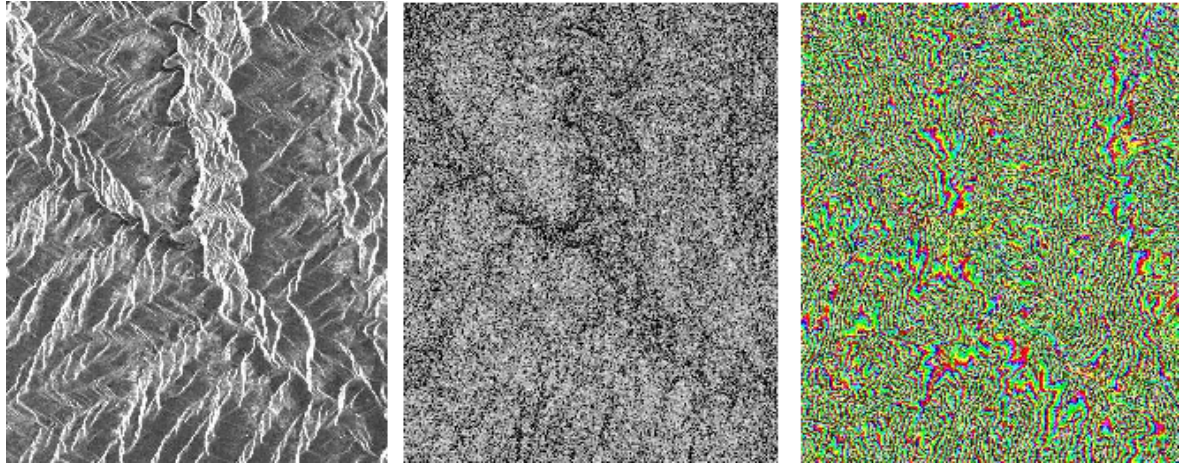
Figure 4.10: Magnitude image, coherence map and interferogram of the Katse area.

Subsequent to the processing of these initial images by JPL, and the commissioning of a processing facility in the Radar Remote Sensing group at UCT, all subsequently acquired data was processed. As data continues to be acquired, there may well be further opportunity to produce useful results in the future, but at this stage, only one pair of images (24980 and 20838) has been suitable for long temporal baseline interferometry (Table 4.1).

It was ascertained that provided that the spatial baseline is small (<30 m), the phase coherence between long time baseline (3 years) ERS data over Lesotho is remarkably good (Figure 4.11), and well within the noise limits for interferometric work. More specifically, this allowed the production of an interferogram (Figure 4.12) using images from April 1996 and April 1999 - a pair containing virtually all of the probable differential effects of crustal loading (Figure 4.9).

In spite of having very high quality Tandem interferograms, it was not possible to unwrap them over large enough areas to be able to generate an InSAR DEM. This is extremely unfortunate, because the resolution and accuracy of such a DEM would have far exceeded the requirements of this project, and would have been a valuable product in its own right. The fundamental reason for this lack of success with InSAR DEM generation was that the topographic relief in the region is such as to cause radar layover & shadow making phase unwrapping possible only in small patches. Without very accurate tie points, these independently unwrapped patches cannot be linked without introducing unpredictable bulk errors.

The DEM, which was generated by combining coarse topographic data and the stereo-SAR DEM (Figure 4.7), was used for removal of the topographic phase. Whilst there remains a strong residual topographic effect in the interferogram due to the inaccuracies of this DEM, there is no evidence of deformation fringes in the resultant differential interferogram (Figure 4.13).

When this interferogram is unwrapped, as far as unwrapping is possible, a linear trend from left to right is apparent. It is possible, but unlikely that this trend could be due to loading effects of the reservoir. Firstly, the effect is too linear in nature from left to right in the image, indicating a probable slight error in the baseline estimate. And secondly, the trend continues to the west of the reservoir. Furthermore, the magnitude of the "linear deformation", 4 fringe cycles or 11.2cm (1 differential fringe equates to half a wavelength of movement), exceeds the values obtained from geodetic monitoring of the survey monuments (Table 4.2), where the maximum deflection is shown to be in the order of 2cm.

The geodetically measured deformation represent both a relief for the designers of the dam, and an answer to the broader questions of crustal, or flexural thickness in the region. Ironically however, it does represent a disappointment with regard to the lack of a result in this project. The viability of the interferometric technique for this project relied on the extent of the deformation being within the limits of a single 100 x 100km ERS scene. As explained in Section 4.4.1, we were fortunate in having a data set which included the entire Katse Reservoir at the edge of the scene, thus giving us the widest possible view of the deformation field. Unfortunately however, the small amount of measured vertical displacement is indicative of a thicker than anticipated crust. This in turn, will have caused, in spite
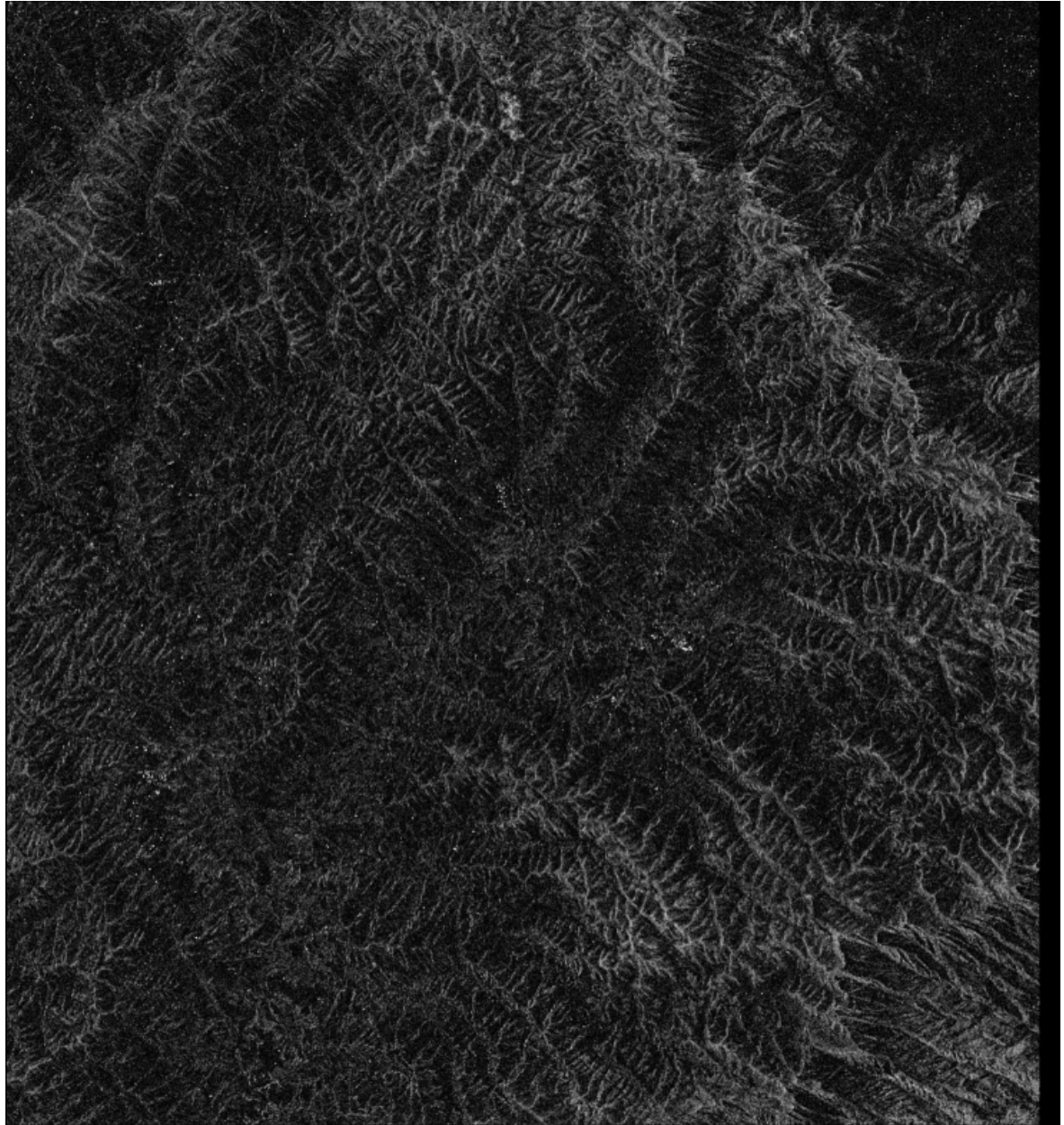
Figure 4.11: Phase coherence over three years, 05307_20838. Brighter shades indicate higher coherence
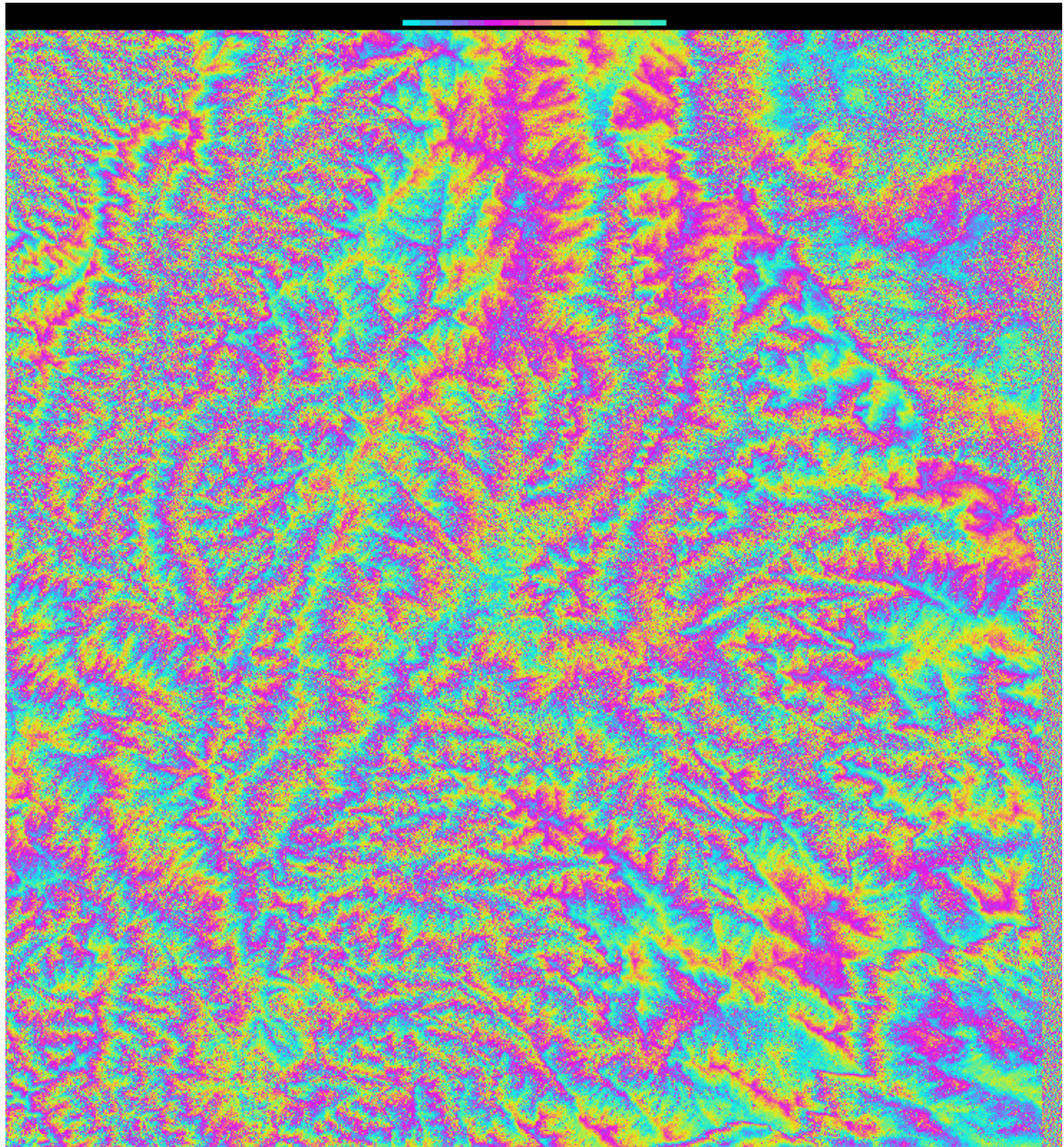
Figure 4.12: Three year interferogram, 05307_20838 (adaptive filter applied)
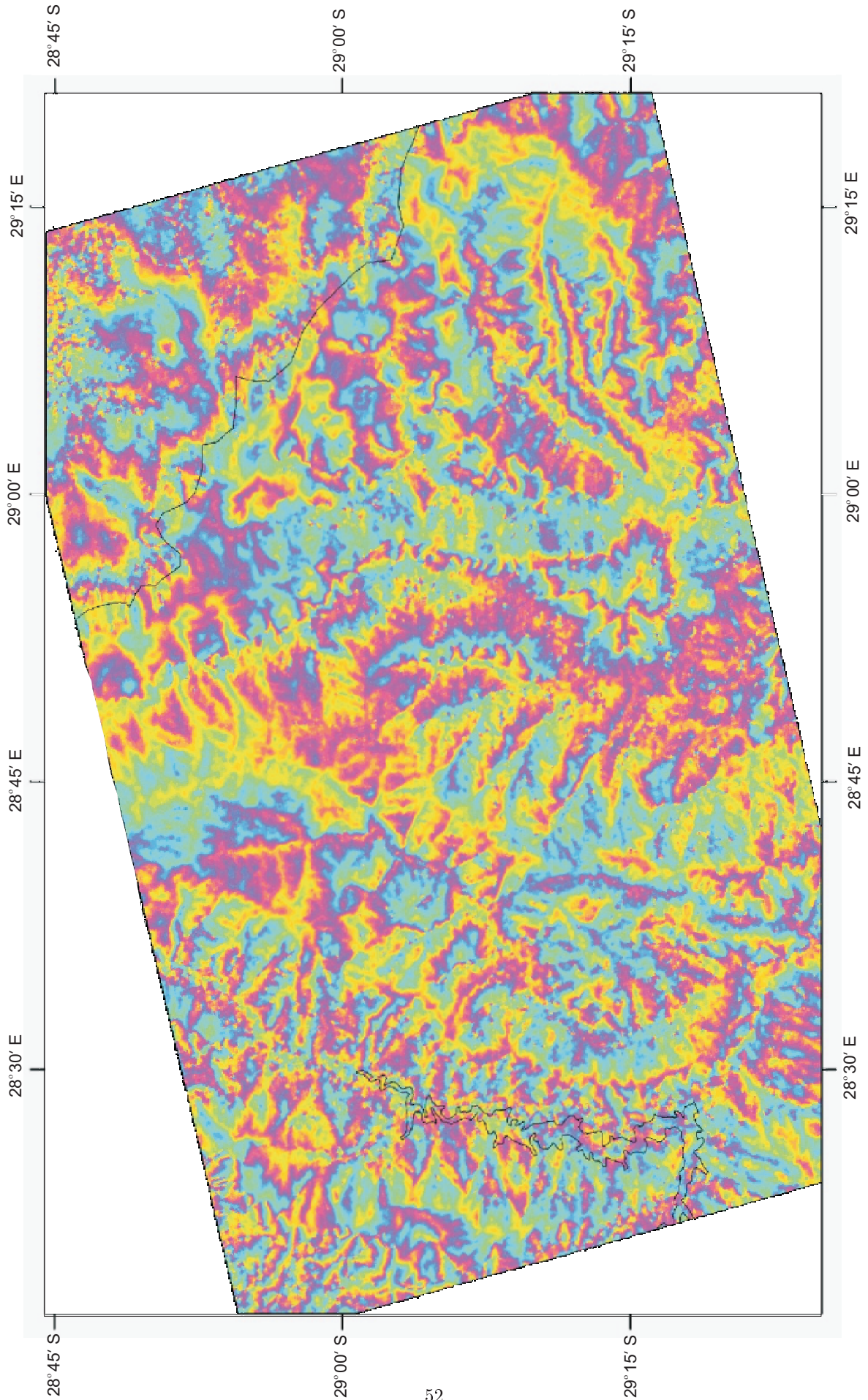
Figure 4.13: Differential phase over three years (with residual topography). Topographic phase contribution removed with coarse DEM. (05307_20838 - DEM)

of a *decrease* in vertical movement, a dramatic *increase* in the effective flexural wave-length, or lateral extent over which the deformation would have taken place.

A deformation radius in excess of 100km will potentially cause a fringe pattern that cannot be seen in a single ERS scene. The scene size is 100 by 100km, so the characteristic circular fringe patterns, such as those derived in the Welkom deformation study (Chapter 5), would not be visible. The only possible option left under these circumstances is to attempt to stitch adjacent (in the same swath) scenes together in order to get a broader view of the area. Since these adjacent scenes were not originally requested for acquisition, many of them do not exist however, and others are only partial images. Interferometric processing of an extended swath was therefore not possible.

In addition to mapping the broad scale deformation, it was had hoped that a study might be included of the smaller scale features such as the surface dislocation due to the Ha Mapeleng seismic event in January 1996. It was hoped that the resulting interferograms would be of sufficiently high resolution to observe active faulting or other non-uniform deformations taking place in the crust around the Katse Reservoir. The isolation of any of these subtle features was not successful, and it is suspected that this may be as a result of their effects being under the phase noise threshold. Phase noise derives from a combination of thermal noise in the instrument system and background radiation. Other contributing factors include the decorrelation due to changes in the viewing geometry and surface characteristics during the imaging process.

4.9   SAR intensity images for lineation analysis

The SAR intensity images were found to be of little value for geological lineation analysis of subtle features. The reason for this is that the nature of the terrain is such as to cause considerable layover and shadow regions in the images. The dynamic range produced by these effects has a strong tendency to obscure the subtle lineations that may be detectable through a careful examination of aerial photos or other optically derived data. The same effect that obscures these subtle features in this sort of terrain, is likely to enhance them in flat or otherwise featureless areas. A high quality DEM such as that which should emanate from the SRTM mission could be an interesting and valuable tool for such an analysis.

4.10   Conclusions and Recommendations - Katse project

This project got off to a slow start, with problems relating to data acquisition, and the lack of an "in-house" processing facility. The flow of data was ultimately secured through a co-operative agreement with UK based researchers and the European Space Agency's announcement of opportunity, AO3. The processing issue has been solved very successfully with the purchase of the Gamma® suite of SAR processors.

Surprisingly good coherence results were obtained over a period as long as three years, and a differential interferogram was generated that ought, based on deformation predictions, to have included the effects of the loading. However, the actual deformation that has taken place, subsequent to the inception of this project, as measured by conventional surveying, indicates that we probably should *not* be seeing any of these effects in the interferogram. A substantial amount (+10cm) of vertical displacement was expected over an area that would have fallen well within a single SAR image, but the subsequent geodetic measurements imply that not only is the vertical movement significantly less than 10cm, but that the loading effect would be distributed over a much larger area.

ERS data is still being acquired for this project, and as a result of the findings that the displacement field could be confused with a linear phase ramp in a single 100 x 100 km image, data to the north and south of the scene containing the reservoir itself is required. Assuming that the appropriate data is acquired, interferograms that span multiple images will have to be processed in the hopes that the apparently linear phase trend will show some curvature centred on the reservoir.

4.10.1 A retrospective geological consideration

Although there is not necessarily a direct correlation between lithospheric thickness and flexural thickness or rigidity, in the absence of other information, the presence of diamondiferous Kimberlites in the region should have raised suspicions. Although Kimberlites are mantle derived rocks, the pressure and temperature conditions required for diamond formation are such as to necessitate an abnormally thick lithosphere. On the basis of mineralogy and chemistry, two types of Kimberlite have been identified in Lesotho [22]. One contains an assemblage of minerals indicative of a formation depth of 100-150km, and the other contains minerals which will have formed under the pressure conditions found at depths between 150 and 200km. Such crustal thickening may be supportive of the postulate that there exists a tectonic suture zone in this region, it does not however rule out the possibility of incipient rifting subsequent to Kimberlite emplacement.

Chapter 5

Welkom Seismic Event

5.1   Introduction

Shortly after midnight on April 23rd 1999, the South African mining town of Welkom was shaken by a magnitude (local) 4.5 earthquake. Hundreds of mine workers were trapped more than a kilometre underground, because of power failures and substantial damage to the Eland shaft of Matjhabeng mine. Miraculously, only two people were killed.

In some cases, the mining of gold in South Africa takes place at depths greater than two kilometres. The pressures at these depths are extreme, and the disturbance to the stress regime by mining activity is the cause of frequent rockbursts and fault remobilisation. The associated mining induced seismicity, although not usually as severe as the April 1999 event, has a devastating effect not only on the miners themselves, but also on the production targets of the mines. For these reasons, the exact causes of and nature of the seismicity, and possible prediction methods have become a hot subject for research by geophysicists and mining engineers.

The imaging of co-seismic displacements by radar interferometry has revealed some spectacular results in the last six or seven years[11][23], but most of these studies have involved earthquakes two orders of magnitude greater than that which occurred in Welkom in April 1999. Here the applicability of the technique to measurements of the deformation associated with deep mining induced rockbursts are demonstrated.

5.2   Image selection and processing

For the purposes of extracting ground movement information from the Welkom scene, a suitable set of radar images was required. The identification of appropriate data was achieved by first locating the epicentre of the earthquake, and then by entering search criteria into the Descw software. The epicentre location was identified by consulting the USGS, National Earthquake Information Centre's (NEIC) database at `http://wwwneic.cr.usgs.gov/neis/epic/epic.html`. This database contains the co-ordinates and magnitudes of all events logged by the global seismic network, a network of seismographs that was originally set up for nuclear test monitoring. The accuracy of fixings depend on the density of monitoring points in the general region of the earthquake, and in South Africa, an error of 10 km in geographic location and 10 km in depth is possible. The South African Council for Geosciences (SACG) provide an independent monitoring service, and their error is roughly the same as that of the NEIC. At a later stage in this project, accurate co-ordinates for the event focus, as recorded by instruments located in the mines, were obtained from ISS through the department of Geophysics at the University of Witwatersrand. The three co-ordinate sets are tabulated below (Table 5.1):

Table 5.1: Welkom event statistics

	NEIC	SACG	Mine instruments
Date	23 April '99		
Time (local)	00:19:36.97	00:19:39.1	00:19:38
Location	-27.953 26.653	-27.80 26.64	-27.9338 26.7128
Depth	5 km	2 km	331 m
Magnitude	5.70 Mb	5.1 (local)	4.5 (local)

5.2.1   Data search and processing

The archived pre-event data included a Tandem ERS image pair from December 1995 (Table 5.2), suitable for the generation of an elevation map of the area. The perpendicular baseline of the the pair 23212-3539 is 378 m, giving it quite a high fringe rate, and consequently making it very sensitive to what little topography there is in the Welkom area. An image was available from October 1998, and since ERS data is not routinely acquired over South Africa, post event data had to be requisitioned. An image was subsequently received in September 1999. Although not ideal for interferometry, because of the long time separations of the images, the spatial separation of the 1998 and 1999 images was well within the limitations of the interferometric technique.

Table 5.2: ERS scenes used for the Welkom deformation study.

Track 178   Frame 4167   Perpendicular baselines

Acq. Date	Orbit	23212	23713	3539	4040	18068	23078	23579	Quality
23-Dec-95	E1-23212	-							11% missing lines
27-Jan-96	E1-23713	263	-						37% missing lines
24-Dec-95	E2-3539	378	116	-					Good
28-Jan-96	E2-4040	252	11	126	-				60% missing lines
04-Oct-98	E2-18068	151	112	227	101	-			Good
19-Sept-99	E2-23078	40	223	338	212	111	-		Good
24-Oct-99	E2-23579	529	266	151	277	378	489	-	Good
28-Nov-99	E2-24080	1503	1240	1125	1251	1352	1463	974	

Although the perpendicular baseline between images 23212 and 23078, a pair spanning the seismic event, is only 40 m, the temporal decorrelation was found to be too high to produce interferometric fringes anywhere other than over the built up parts of Welkom itself. There are two reasons for this decorrelation. The first is that, judging by the amount of water present in the December 95 image, it must have been raining at or around the time of acquisition. The presence of increased surface water is evident by comparing these December images with others from September and October (dry season). The river courses and pans are markedly larger, and show the low backscatter typical of water bodies. The second probable cause of decorrelation is extensive agricultural activity that takes place in this region. The variation in crops or pasture characteristics invariably cause complete decorrelation.

The pair which was found to be most suitable for extraction of the differential movement was the pair 18068-23078, with a baseline of 111 m, and with reasonably good coherence due to them both having been acquired at about the same, dry, time of year. In spite of agricultural activities, and a long time baseline (11 months) though, temporal decorrelation was sufficiently low in the Welkom scene for us to be able to generate a differential interferogram of the deformation which took place in the intervening time . The Welkom area is extremely flat, and it was possible to extract the differential movement (Figure 5.1) from this pair purely by eliminating the residual (flat Earth) phase component from the interferogram. This was achieved by means of Fourier Transform filtering the periodic signal component from the interferogram.
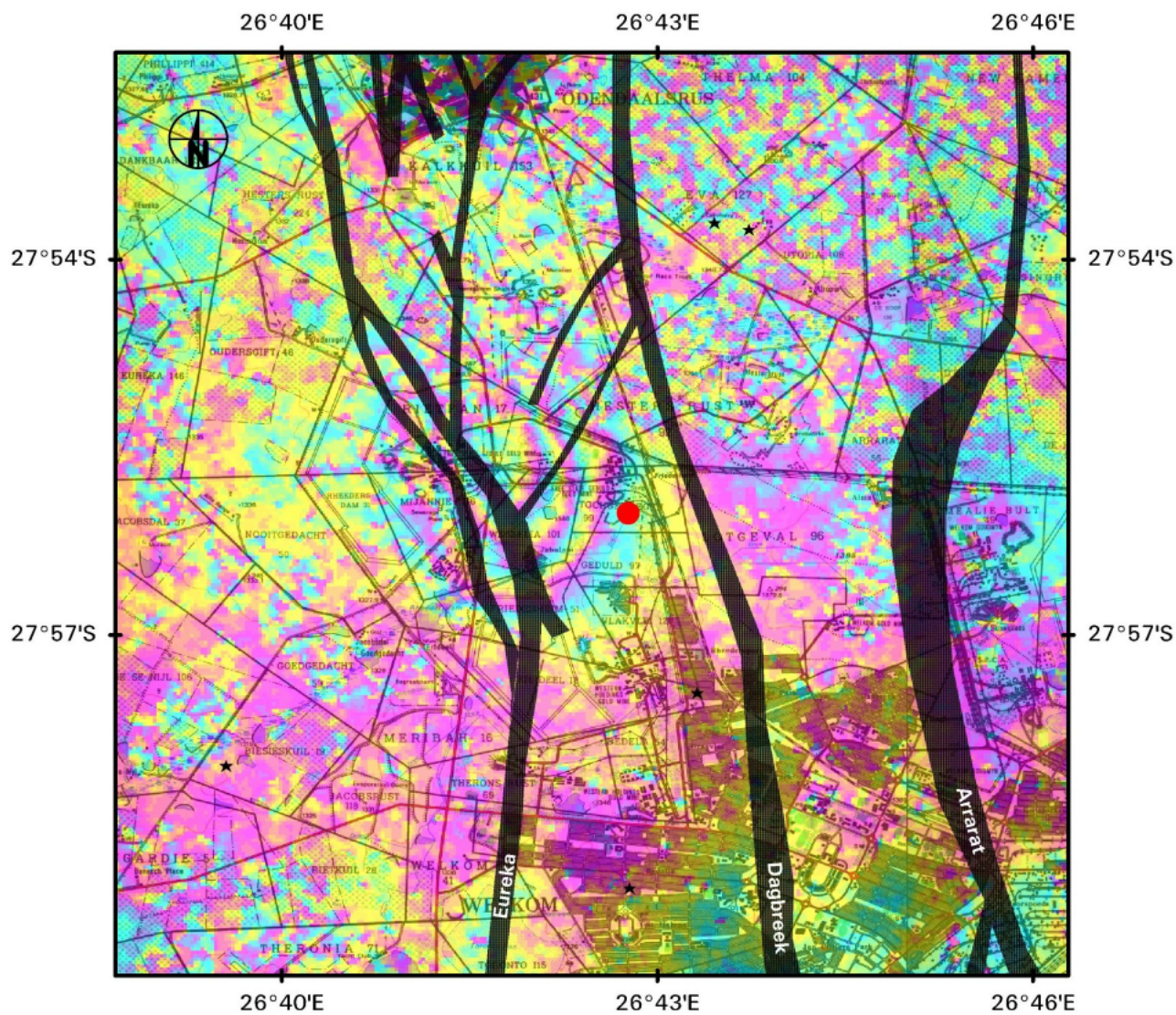
Each interferometric fringe represents 26mm of vertical
ground displacement which resulted from the
April 1999 magnitude (local) 4.5 earthquake in Welkom

●   Earthquake epicentre

★   Other Mag > 4 events since 1971

       Major fault zones

Scale

2000   0   2000   Meters
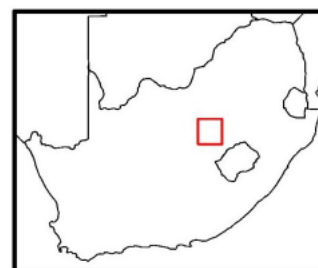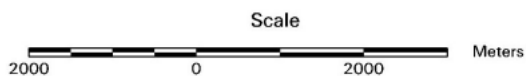
SAR processing and interferogram - G. Doyle
Radar Remote Sensing Group
University of Cape Town

Figure 5.1: Differential interferogram of ground deformation in the Welkom gold fields

5.3   Result and discussion

The elliptical fringe pattern in the interferogram (3.5 to 4 fringes) represents approximately 9.5 cm of vertical displacement at the centre. The length of the ellipse, which is oriented parallel to the major geological structures, is 5.2 km. The position of this deformation feature coincides with the Eland Shaft of the Matjhabeng mine, which was worst affected by the earthquake, and with the focus of the event. Its orientation and magnitude also coincide with the major geological structures, particularly the Dagbreek fault zone, which dips steeply to the west [24]. If projected onto the plane of the Dagbreek fault zone, the shape and magnitude of the interferometric fringe pattern is consistent with an average slip on the fault of ~10 cm.

5.4   Conclusion

The time span between image acquisitions is relatively long (11 months), and since general ground subsidence due to the mining activities is prevalent in this area, this cannot be ruled out at least as a contributing factor in the deformation process. There is however, a strong correlation between the calculated deformation for an event of the type that occurred in Welkom in 1999 and that measured by interferometry. This lends strong support for the possibility that the surface movement as measured by satellite interferometry may provide valuable feedback on the accuracy of rock behavior models and deep mining rock-burst dynamics.

Chapter 6

Summary and Conclusions

The construction of a DEM of the Western Cape by interferometric SAR turned into a very useful demonstration not only of the potential, but also of the limitations of the technique. There are elements of the processing technique that need to be refined. For example, an automated technique is required for integrating existing, coarse, but accurate DEMs, or ground control into the InSAR process so as to facilitate the phase unwrapping procedure (unwrapping guidance). Methods for combining height information derived from independent image pairs, acquired from different perspectives will contribute significantly to the elimination of errors due to layover and atmospheric perturbations.

The success of the Katse project was limited by the fact that the crustal deformation which has taken place due to the filling of the Katse reservoir is not sufficient to be within the detection capability of the InSAR technique. Surprisingly good coherence results were obtained over a period as long as three years though, and a differential interferogram was generated that ought, based on deformation predictions, to have included the effects of the loading. The ability to generate interferograms over this time period, and in this type of terrain is extremely encouraging for the viability of the technique in other applications.

The area and magnitude of the surface deformation that resulted from the April 1999 earthquake in Welkom was very successfully delineated by differential InSAR. This hopefully provides strong support for the use of this technique in ameliorating the effects of rock-bursts in mining operations.

Because of the great number of conditions for the viability of SAR interferometry it is struggling to find its way into general commercial application. Part of the problem is that the theoretical concepts surrounding the technique are not simple, thus causing general apprehension towards its use.

Bibliography

[1] L. J. Cantafio, ed., *Space-Based Radar Handbook*. 685 Canton Str. Norwood, MA 02062: Artech House, Inc., 1989.

[2] S. Hovanessian, *Radar System Design and Analysis*. 685 Canton Str. Norwood, MA 02062: Artech House, 1984.

[3] A. K. Gabriel, R. M. Goldstein, and H. A. Zebker, "Mapping Small Elevation Changes Over Large Areas: Differential Radar Interferometry," *Journal of Geophysical Research*, vol. 94, pp. 9183–9191, July 1989.

[4] A. J. Wilkinson, *Techniques for 3-D Surface Reconstruction using Synthetic Aperture Radar Interferometry*. Ph.d. thesis, University of London, 1997.

[5] T. Dixon, "SAR Interferometry and Surface Change Detection," *http://southport.jpl.nasa.gov/scienceapps/dixon/index.html*, 1995. Report on a workshop held in Boulder, Colorado: February 3-4, 1994.

[6] D. Massonnet and K. Feigl, "Radar Interferometry and its Application to Changes in the Earth's Surface," *Reviews of Geophysics*, vol. 36, no. 4, pp. 441–500, 1998.

[7] H. A. Zebker, P. A. Rosen, and S. Hensley, "Atmospheric Effects in Interferometric Synthetic Aperture Radar Surface Deformation and Topographic Maps," *Journal of Geophysical Research*, vol. 102, pp. 7547–7563, April 1997.

[8] SRTM Project Office, JPL, "SRTM: Mapping the World in 3 Dimensions." http://www.jpl.nasa.gov/srtm/, 2000.

[9] H. Gupta and B. Rastogi, *Dams and Earthquakes*. New York: Elsevier Sci. Pub. Co., 1942.

[10] P. Wright and R. Stow, "Detecting mining subsidence from space," *Int. J. Remote Sensing*, vol. 20, no. 6, pp. 1183–1188, 1999.

[11] D. Massonnet, M. Rossi, C. Carmona, F. Adragna, G. Peltzer, K. Feigl, and T. Rabaute, "The displacement field of the Landers earthquake mapped by radar interferometry," *Nature*, vol. 364, pp. 138–142, July 1993.

[12] D. Massonnet, P. Briole, and A. Arnaud, "Deflation of Mount Etna Monitored by Spaceborne Radar Interferometry," *Nature*, vol. 375, pp. 567–570, June 1995.

[13] D. MacKellar, "The design and construction of katse dam," *Civil Engineering*, vol. 2, no. 9, pp. 11–14, 1994. S. Afr. Inst. Civ. Eng. Mag.

[14] C. Merry, "Monitoring Potential Vertical Crustal Motion in Lesotho," in *Proceedings of Fourth International Symposium on Recent Crustal Movement in Africa, Nairobi*, (Private Bag Rondebosch), pp. 1–13, Department of Surveying, University of Cape Town, November 1994.

[15] C. Hartnady, "Seismicity and plate boundary evolution in southern africa," *S. Afr. J. Geol.*, vol. 93, no. 3, pp. 473–484, 1990.

[16] F. Fitch and J. Miller, "Potassium-argon radioages of karoo volcanic rocks from lesotho," *Bulletin of Volcanology*, vol. 35, pp. 64–84, 1971.

[17] C. Hartnady, "Uplift, faulting, seismicity,thermal spring and possible incipient volcanic activity in the Lesotho-Natal region, SE Africa: The Quathlamba hotspot hypothesis," *Tectonics*, vol. 4, pp. 371–377, 1985.

[18] C. DeMets, R. Gordon, D. Argus, and S. Stein, "Current plate motions," *International Journal of Geophysics*, vol. 101, pp. 425–478, 1990.

[19] Alex L. du Toit, "Crustal movements as a factor in the geographical evolution of South Africa," *S. Afr. geograph. J.*, vol. 26, pp. 3–20, 1933.

[20] P. Keary and F. Vine, *Global Tectonics*. Oxford: Blackwell Scientific Publications, 1990.

[21] F. W. Leberl, "Radargrammetry," in *Manual of Remote Sensing* (F. M. Henderson and A. J. Lewis, eds.), vol. 2, ch. 4, pp. 183–269, New York: John Wiley and Sons, 3rd ed., 1998.

[22] F. Boyd and P. Nixon, "Origin of ilmenite-silicate nodules in kimberlites from Lesotho and South Africa," *In P.H. Nixon, (ed.), "Lesotho Kimberlites"*, pp. 254–268, 1973.

[23] D. Massonnet, K. Feigl, M. Rossi, and F. Adragna, "Radar Interferometric Mapping of the Deformation in the Year After the Landers Earthquake," *Nature*, vol. 369, pp. 227–230, 1994.

[24] W. E. L. Minter, W. Hill, R. Kidger, C. Kingsley, and P. Snowden, "The welkom gold field," in *Mineral Deposits of Southern Africa* (C. Anhaeusser and S. Maske, eds.), pp. 497–539, Geol. Soc. of S. Afr., 1986.

Appendix A

Katse ERS data archived at UCT
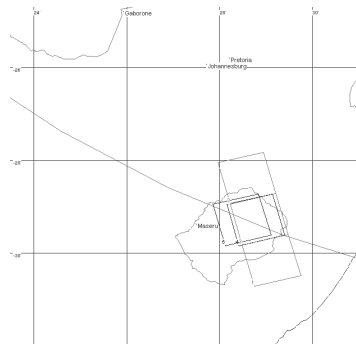
Mission	Date	Track	Frame	Orbit	Type	PAF
ERS-1	04-jul-94	602	6597	15523	PRI	DLR
ERS-1	16-sep-94	1664	6597	16585	PRI	DLR
ERS-1	06-dec-95	443	6597	22976	RAW	ESRIN
ERS-1	10-jan-96	443	6597	23477	RAW	ESRIN
ERS-1	24-apr-96	443	6597	24980	RAW	ESRIN
ERS-2	07-dec-95	443	6597	03303	RAW	ESRIN
ERS-2	11-jan-96	443	6597	03804	RAW	ESRIN
ERS-2	25-apr-96	443	6597	05307	RAW	ESRIN
ERS-2	15-apr-99	443	6597	20838	RAW	ESRIN
ERS-2	20-may-99	443	6597	21339	RAW	ESRIN
ERS-2	24-jun-99	443	6597	21840	RAW	ESRIN
ERS-2	02-sep-99	443	6597	22842	RAW	ESRIN
ERS-1	06-dec-95	443	6579	22976	RAW	ESRIN
ERS-1	10-jan-96	443	6579	23477	RAW	ESRIN
ERS-2	07-dec-95	443	6579	03303	RAW	ESRIN
ERS-2	11-jan-96	443	6579	03804	RAW	ESRIN
ERS-1	06-dec-95	443	6615	22976	RAW	ESRIN
ERS-1	10-jan-96	443	6615	23477	RAW	ESRIN
ERS-1	24-apr-96	443	6615	24980	RAW	ESRIN
ERS-2	07-dec-95	443	6615	03303	RAW	ESRIN
ERS-2	11-jan-96	443	6615	03804	RAW	ESRIN
ERS-2	25-apr-96	443	6615	05307	RAW	ESRIN

Appendix B

Processing the Cape ERS scenes with the Gamma software

A brief explanation is provided for each step, but a more thorough insight may be obtained by referring to the Gamma documentation.

Five basic steps followed in this case study, for the production of a topographic map with SAR data:

1. MSP Processing - Process the RAW data to produce Single Look Complex (SLC) images.

2. ISP Processing - Generate the interferogram.

3. Phase Unwrapping

4. Height Map - Produce a calibrated, georeferenced height map from the unwrapped phase.

5. Quality assesement and filtering.

B.1 MSP - Processing to SLC

The selection of data pairs for interferometry is an important process, which is discussed in (Section 3.3). Presented here, is the procedure that was followed for the subsequent processing of scene 05715 (ERS-2 data).

1. **Preliminary setup**
   a) The convention is to name working directories according to the orbit number of the scene being processed.
   b) The antenna pattern file, ERS2_antenna.gain, was copied from MSP/sensors directory to the working directory.
   c) The appropriate raw data/sensor parameter file (ERS2_ESA.par) was also copied from the same directory.
   d) The MSP processing script (ERS_PROC) was copied from the MSP/scripts directory to the working directory.
   e) The RAW data and leader file was extracted from CD onto hard drive for processing.

2. **Generating Gamma image parameters file** (p05715.slc.par) **(example in Appendix F).**
   The leader file reader for the Italian PAF (ASI) worked the best for this SAC archived data. Others were tried, but with varying success in extracting the relevant information from the CEOS leader file.

ERS_proc_ASI 05715.ldr p05715.slc.par

Although the ASI reader worked the best, it was still unable to extract the correct image start time from the leader file.

3. **Correcting the errors in the parameters file**
   Using a software utility obtained from ESA, and adapted by Andrew Wilkinson (RRSG - UCT), the CEOS leader, which is a in a mixed binary and ASCII format, was extracted to an ASCII text file (Appendix E) for manual extraction of the relevant information.
   (Yak about the errors in the SAC header & how to fix the gamma par file)

4. **Identifying and downloading the appropriate PRC orbits file.**
   (Where are they? Delft and ESA/DLR orbits. Ref web pages & ftp sites (note DLR orbits not accessible to general public)

5. **Tweaking the state vectors with the PRC orbits.**
   This definitly won't work until the image start time has been corrected in the par file. This is how I knew there was something wrong with the par file.

   PRC_proc p05715.slc.par PRC_960519_05652_rev2

   (what does this actually do?)

6. **Cleaning up the RAW data (missing line interpolation).**

   ERS_fix ERS/ESRIN ERS2_ESA.par p05715.slc.par 0 05715.raw 05715.fix

   (comment on the disk I/O thing & reading & writing from/to different disks for all processing This general philosophy should be observed whenever possible.) (On Gollach this only really holds true if the disks are on the same node - this very specific to RRSG?).

   For ERS data, the cross correlation switch should be turned off. If it is switched on, the detector is likely to incorrectly detect missing lines, thus generating spurious lines and cocking it all up! The ERS line counters are reliable.

   Output: 05715.fix

7. **Processing RAW data to SLC (show all steps and describe the process - what are the outputs?)**
   (ERS_PROC can be used, but rather yak about the subroutines individually.)

   ./ERS_PROC ERS2_ESA.par 05715 2 10 (set write directories here) 4096

   Alternatively.... (all the subroutines)

   (Comment again on the size of the RC and SLC files, and how best to handle them.)

   (What are the input parameters here?
   ERS2_ESA.par file
   Range and azimuth looks (This affects the amount of disk space used, and the speed of processing in subsequent steps. Selecting 2 x 10 looks, the process "averages" every 2 line along range (x) and every 10 lines along azimuth (y). For a full resolution image, the initial number of lines is range=4912 and azimuth=27200. With 2 by 10 looks, the resulting size is range=4912 and azimuth=5440. Of course, the SLC is not affected

Read/write directories
etc.

Outputs:
05715.slc
05715.mli
p05715.mli.par
05715.rc
autof1.mli
autof2.mli
autof_05715.out
az_05715.out
azsp_05715.out
mli_05715.out
pre_05715.out
rspec_IQ_05715.out
auto.cc
05715.autof
05715.azsp
05715.rspec

(Possible problems with ERS_PROC and their solutions)

8. **A quick quality check to see if things went well.**
   Check p.05715.mli.par to get the correct image size.

   Make a raster file of 05715.mli and view the image. Check for blurring, etc. missing lines may present a problem, but only if there are lots of them. The SAR processing is robust in situations of missing data (explain?). Missing lines will however cause a decrease in correlation between images during InSAR processing.

9. **The above steps repeated for other image (25388).**
   Keeping in mind that scene 25388 was acquired with the ERS1 satellite.

B.2 ISP - Interferogram production

Interferometric processing is not simply a case of following a recipe. There are many alternative ways of processing SAR data, and in general, the methods used will depend on factors such as the PAF's own particular flavour of CEOS and the nature of the terrain. The processing alternatives are discussed in the Gamma documentation, but the procedure followed for this study was as follows:

1. **Preliminary setup**
   a) An alternative disk to the one containing the SLCs was sought (to optimise speed).
   b) Again, following convention, the ISP directory 05715_25388 was made, and soft links to the .slc files included.
   c) The p05715.slc.par and p25388.slc.par files were copied to the ISP directory.
   d) The selection of 05715 as the master image was based on the optimisation of baselines with other possible images in archive (according to the ESA database).

2. **Creating the SLC parameter file: 05715.slc.par**

   par_MSP ERS2_ESA.par p05715.slc.par 05715.slc.par

   The same was done for 25388

The ISP can be run with the INTERF_SLC script, but the running of the routines individually is discussed below.

3. **Creating offsets file**

   create_offset 05715.slc.par 25388.slc.par 05715_25388.off 1

   The "1" at the end is a switch used to tell create_offset to use the image intensity cross correlation rather than fringe visibility (2) to arrive at the offsets.

   Controlling what areas you are processing is done in create_offset. If you have a missing line in the middle of your image, and want to process the top and bottom halves separately, then change the azimuth position in these lines (The location of missing lines can be obtained from your MSP log files - the ERS_fix routine generates a report of these things.

4. **Estimating initial offsets.**

   init_offset 05715.slc 25388.slc 05715.slc.par 25388.slc.par 05715_25388.off 2 5

   init_offset 05715.slc 25388.slc 05715.slc.par 25388.slc.par 05715_25388.off 1 2

   init_offset 05715.slc 25388.slc 05715.slc.par 25388.slc.par 05715_25388.off 1 1

   This takes a small window (in the center of the image by default) and calculates an initial estimate of offset between the two scenes. One of the last output lines is the offset estimate. The offset estimate for range should be in the single digits, whilst the offset in azimuth (lines) can be hundreds of lines.

   Output: 05715_25388.off The ISP parameter file

   (What problems might be encountered with init_offset and their solutions?)

5. **Precision estimate of offsets (Image registration)**

   The "1" as an input parameter in create_offset implies that offset_pwr should be used. Otherwise offset_SLC would be used (check Gamma docs for the differences).

   offset_pwr 05715.slc 25388.slc 05715.slc.par 25388.slc.par 05715_25388.off 05715_25388.offs 05715_25388.snr

   The SNR should mostly be well above the threshold (7 by default - set in create_offset). If not, you will need to return to stage 4 and set the window and FFT a bit larger. (this section warrents much discussion).

   The screen output gives one an indication of whether the registration is likely to be successful. (no of offsets above threshold, etc.)
   Number of valid offsets: should be in the 20s and 30s or more.

   For this particular pair of images, the range offset should be around 5 (largely baseline dependent), and Azimuth offset should be around 1600 (depends on who's controlling the on-off switch!).

   Outputs:
   05715_25388.snr
   05715_25388.offs

6. **Determination of offset polynomials** (based on least squares error method)

   offset_fit 05715_25388.offs 05715_25388.snr 05715_25388.off 05715_25388.coffs 05715_25388.coff-sets 1

   The "1" parameter allows for interactive culling of offsets. The default is "0"
   SNR threshold: left at 7 (the default) to start with, bit raised to 10 after ascertaining that the SNR with this Tandem data is high. This done to imrove the offset fit. (explain)
   Set range and azimuth error thresholds: 3 times the standard deviation given on screen seems to be appropriate (explain).
   After inserting these numbers, Gamma shows the new standard deviation for range and azimuth fits. These values should be less than 0.5. If not, alter thresholds again.

   Outputs:
   05715_25388.coffs
   05715_25388.coffsets

7. **Computing normalised interferogram and registered intensity images**

   interf_SLC 05715.slc 25388.slc 05715.slc.par 25388.slc.par 05715_25388.off 05715.pwr 25388.pwr 05715_25388.int 1 5

   Outputs:
   05715.pwr (registered intensity image averaged according to rlks and azlks.)
   25388.pwr
   05715_25388.int (unflattened interferogram)

   The .pwr images are used in conjunction with the .cc image to pick ground control points later.

8. **Creating Sun raster files and inspection of the results**

   raspwr 05715.pwr 4912
   raspwr 25388.pwr 4912
   rasmph 05715_25388.int 4912 1 5440 1 1 2.0 0.3 1

9. **Calculating the baseline**
   There are three ways of calculating baseline, from the state vectors, by FFT calculation of average fringe rate, and from the offsets. Combinations of these can be used for parallel and perpendicular baseline estimation. (explain this step carefully, particularly wrt Welkom processing).
   The object of calculating baseline and the next step is to subtract flat earth phase (insert ref to text).

   base_init 05715.slc.par 25388.slc.par 05715_25388.off 05715_25388.int 05715_25388.base 2

   Before it gets going, base_init gives an indication of which method is most appropriate, (or at least, which method will or won't work). Here I used option 2, which estimates the parallel baseline from the state vectors, and the perpendicular baseline using an FFT in the range direction.

   Output: 05715_25388.base

10. **Subtraction of the flat earth phase:** (making the flattened interferogram).

67

ph_slope_base 05715_25388.int 05715.slc.par 05715_25388.off 05715_25388.base 05715_25388.flt

A Sun raster image was made for visual inspection of the product.

rasmph 05715_25388.flt 4912 1 5440 1 1 2.0 0.3 1

Output:
05715_25388.flt
05715_25388.flt.ras

11. **Making the correlation map.**

cc_wave 05715_25388.flt 05715.pwr 25388.pwr 05715_25388.cc 4912 5

This maps the phase cross correlation between the images (correlation range 0 -1).

Output:
05715_25388.cc

Generate a Sun raster cc image. The color range is from blue to purple to yellow. Blue is the lowest, purple is medium, and yellow is highest correlation.

rascc 05715_25388.cc 05715.pwr 4912

B.3   Phase unwrapping and height map generation.

Flags, neutron, grasses, etc. Incl. precision baseline estimation using GCPs (Bridges & GCP txt file formats?). Note all the pitfalls and thresholds that have to be carefully optimised.

Blab on about all the trade-offs and compromises here. Thresholds, branch lengths, neutrons.

1. **Smoothing the fringes** (adaptive filtering of interferogram)

adapt_filt 05715_25388.flt 05715_25388.flt.sm 4912

inspection of the product (sun ras image:)

rasmph 05715_25388.flt.sm 4912 1 4924 1 1 2.0 0.3 1

Output:
05715_25388.flt.sm & .ras

Problems? (blank image - not sure why, but decreasing the no of processed lines fixed the problem).

2. **Masking of low correlation areas.**

corr_flag 05715_25388.cc 05715_25388.flag 4912 0.3

Areas of low correlation should be avoided during the unwrapping process, so these areas must be identified and masked during initial unwrapping.

Experimented with the correlation threshold to unwrap the maximum area without errors. This is a highly interactive process, requiring much gazing at images, and of course, much prior

knowledge!

The fraction LSNR points gives an indication of how much of the interferogram will potentially unwrap, but I found the trial and error method for the Cape scene to be more appropriate. (why). Letting the LSNR go too low will cause phase unwrapping errors. These will be evident in the unwrapped product as clear dislocations.

Output: 05715_25388.flag

rasbyte 25388_05715.flag 4912 can be used at any time in the next few steps to create a ras image of the flag file for viewing.

3. **Neutrons**
(what are they, and how does it all work)

neutron 05715.pwr 05715_25388.flag 4912 6

4. **Determining the residues.**

residue 05715_25388.flt.sm 05715_25388.flag 4912

5. **Connecting residues.**
There are two methods for generating branch cuts, tree_cc and tree_gwz (method by Goldstein, Zebker, and Werner insert the ref.). tree_gwz is more conservative, since it allows branch cuts to cross, thereby excluding some regions. I used this one.

tree_gzw 05715_25388.flag 4912 32

The default maximum branch length is 32, but through experimentation (repeated runs of tree_gzw) I found that I could derease this to 28, thereby slightly increasing the unwrapped area.

6. **Phase unwrapping**
The starting position for phase unwrapping is the centre of the scene by default. A better starting point was however determined by inspection of (cc & int).

Unwrapping takes the phase measurements, which are modulo 2pi ambiguous, and adds them up from the start to determine the cumulative phase change across the scene. By default, the unwrapping is started at the centre of the scene, but this might be entirely inappropriate (low coherence - water, etc.), so, the coherence map and the flattened interferogram wre examined for a high quality region in which to start (nice flat, large unwrappable area). A few attempts at unwrapping were required before the optimum starting point was found.

grasses 05715_25388.flt.sm 05715_25388.flag 05715_25388.flt.unw 4912 (0 4912 0 4924 3500 2500)

Output: 05715_25388.flt.unw

The unwrapped image and the flag file have to be deleted before returning to step 2 to retry the unwrapping with different parameters.

I found it easiest to import the .unw image into ERDAS to examine it for bulk errors - unwrapped phase dislocations. Also imported the .cc file for examination in conjunction with the unwrapped phase. This helps to determine the appropriate corr_flag threshold. A look at the .cc image statistics also helps.   (explain all this).

7. **Construction of bridges.**
   (What is the purpose of this step - and how does it work)

   rastree 05715_25388.flt.sm 05715_25388.flt.unw 05715_25388.flag 4912 1 4925 0.25 05715_25388.flt.bridge.ras

   xv 05715_25388.flt.bridge.ras &

   An ASCII bridge file has to be generated with a text editor: (what is the format?)

   rasrmg 05715_25388.flt.unw 25388.pwr 4912

   xv 05715_25388.flt.unw.ras &

8. **Choosing ground control points.**
   GCPs provide control for the acurate estimation of the baseline, and the subsequent removal of any residual tilt from the unwrapped phase image. About 12 points are needed, spaced out across the scene (low order polynomial, so more will not help).

   Create a gcp txt file in the form (gcp# rng az hgt)

   (comment on this being an alternative to the Gamma tools, which don't work in the RRSG environment.)

   Use either of the registerred power images. In xv, pixel co-ordinated can be obtained by clicking with the center mouse button on the point that you have identified.

   Topo maps may be used to identify elevation points, but rigorous gcp collection in the field should give a more accurate product.

   Comment on the location of GCPs in amongst atmospheric aberations!

9. **Calculate baseline from GCPs.**
   Extract unwrapped phase at GCPs from interferogram.
   gcp_phase 05715_25388.unw 05715_25388.off 05715_25388.gcp 05715_25388.gcp_data 5
   5 is the default size of the window used for phase averaging.

   base_ls 05715.slc.par 05715_25388.off 05715_25388.gcp_data 05715_25388.base 1 4
   The 4 is the number of terms to solve for in the non-linear least squares estimate: usually 3-5, 4 is the default.

   base_ls rewrites the baseline file with the precision baseline coordinates.

   On running base_ls, look around the first GCP listing for WARNING: GCP not unwrapped. This means that a GCP is located in a spot that was not unwrapped, so it cant be used. Delete this GCP from the GCP file, or make sure that you have located it correctly, and run base_ls again. GCPs should be selected so that this does not happen.

   The height error for the GCP points is listed and should not be any more than, say 40. If it is, delete it in jcc. Remember that you still need about a dozen: (this approach is questionable - but remember that the polynomial being fitted through the GCPs is of a low order - check on this). It may be necessary to go back and get more GCPs if you the number of high error points is high.

   Mean square height error: last output line, want it to be no more than 10 - 20m.

10. **Check result of improving baseline**

(how)

ph_slope_base uses the initial baseline entries and ignore the precision baseline entries.

B.4 Orthorectification and Georeferencing

With and without independent DEM (Power image simulation and registration by cross-correlation)

1. **Make the height map.**
   Slant to ground range conversion, and phase to height conversion.
   hgt_map 05715_25388.unw 05715_25388.flag 05715.slc.par 05715_25388.off 05715_25388.base 05715_25388.hgt 05715_25388.gr

   Outputs:
   05715_25388.hgt
   05715_25388.gr (cross track ground ranges on a spherical Earth)

   use rashgt to make ras image, then view output

2. **Convert to orthonormal coordinates.**

   res_map 05715_25388.hgt 05715_25388.gr 05715.mli 05715.slc.par 05715_25388.off 05715_25388.rhgt 05715.rmli 05715_25388.slope

   (explain orthonormalisation)

   Outputs:
   05715_25388.rhgt
   05715.rmli
   05715_25388.slope

   This is the finished product. The "fringes" represent the contours of a conventional topographic map. The image should have been flipped to its real orientation.

B.5 Product evaluation and "improvement"

ERDAS tricks and the "magic InSAR DEM fixer (insert flow diagram)" (The better the independent DEM, the better the InSAR DEM!)

Difference maps

profiles

looking for phase dislocations

smoothing and subtracting the difference to "correct" the atmospherics and residual baseline error.

Filling the holes (interpolate or combine DEMs)
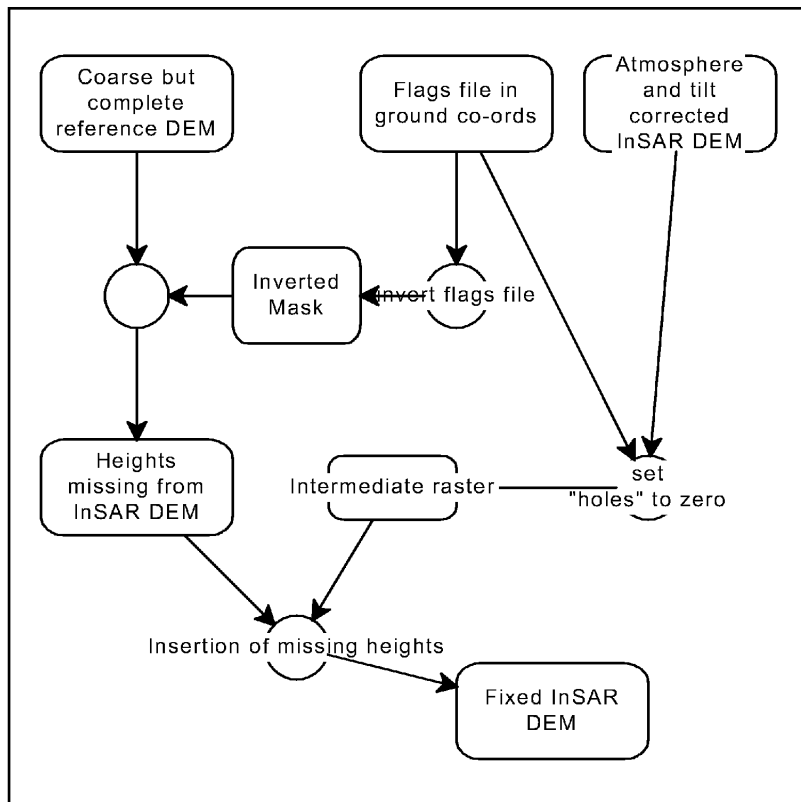
Figure B.1: InsAR DEM hole filler

Appendix C

Katse processing particulars

Don't reproduce processing detail. Just things specific to the Katse processing.

Which scenes, and why. What worked, and what didn't work. (the basic philosophy is to process everything that stands a chance of being useful).

Put everything in chronological order.

The Katse data became available during the course of the project, and only preliminary processing (before filling of the reservoir) was possible at the beginning.

Tandem Scenes processed first, because they were available, and the dam not full yet.

Then, luck sent us an image in (date - post filling) which had a small baseline (20 something metres) with an image of 3 years earlier.

Talk extensively on data selection and timing.

1. Tried to generate height map from Tandem data (procedure as above, but discuss results and problems).
   Using the same method detailed in appendix B
   23477_03804 (122m) Jan '96 Tandem pair (Table 4.1) (includes some filling and the Jan 3 seismic event)
   24980_05307 (92m) April '96 Tandem pair (includes some filling, but still below mol (Figure 4.9) and the Jan 3 seismic event).

   Phase unwrapping problems encountered:
   With thresholds (coherence, neutrons and branch lengths) set at default values, the scene is clearly segmented into small, non-contiguous pieces. These thresholds were tinckered with in turn and in combination, and although it was possible to get larger areas to unwrap, it was fundamentally not possible to determine the efficacy of this procedure. In other words, it was possible to get two or more previously non-contiguous patches to unwrap as one, but it was not possible to ascertain the extent to which this treatment was introducing bulk errors. Some errors were obvious, their magnitudes remained unknown. The conclusion was arrived at quite quickly that ERS SAR is not ideal for DEM generation in this sort of terrain. The areas of layover are too extensive.

   An attempt was made at constructing bridges (Appendix B.3), so as to link independently unwrapped patches, but this did not work at all for the following two reasons: a.) The amount of terrain distortion is extreme, and because of the deep valley, and layover separated regions, it was not possible even by visual inspection to find phase continuity across branch cuts.

   So, the next step was to find some other means by which to generate/simulate the topographic phase component.

2. StereoSAR DEM generation (discussed in section 4.5)

3. Stereo DEM inserted into coarse DEM for purposes of topographic phase removal. Didn't work. Why? Dem to coarse and too noisy. Simulated intensity image only bore a slight resemblance to the true thing, and cross correlation with ERS image wasn't possible.

4. Luck! Small baseline and reasonable correlation over 3 years (this has been discussed already, but the actual details need to be inserted here). i.e. Image numbers, dates, processing procedure (exactly

Appendix D

Welkom processing particulars

Generated Tandem Interferogram with 23212 & 03539 (December '95 pair) note the 11% missing lines in 23212 (appears to be every other line) - low coh band in interferogram, but mli looks fine (attests to the robust nature of sar processing). The plan was to use this interferogram for the removal of the topographic component, but on processing 18068_23078 (note all the procedures used to get it to register - particularly starting point for init_offset), it was found that the differential movement was immediately obvious (in the expected position too) - Didier Massonnet and others have previously commented that where differential movement has taken place, there is usually no mistaking it in an interferogram. It sticks out like a sore thumb.

Procesing parameters, window sizes, etc. Also starting position for FFT

Show before and after images of the interferogram (with and without local FFT flattening) Show the oddities. Show the cc images? Maybe some of these should go into the body of the text.

Standard processing as in Appendix B (not differential) i.e. no removal of topographic phase component by means of independent DEM or third image. Not that this was not possible, in fact, the Tandem pair was excellent for DEM production (apart from the 11% dropped lines). The free state is flat, so simple removal of the average fringe rate sufficed, or should have. It did once the centre location was established for the FFT.
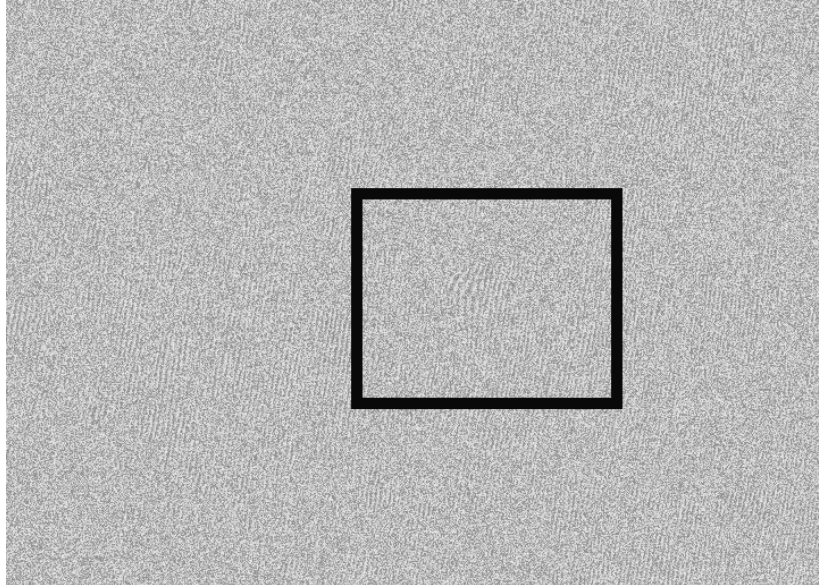
(a) unflattened
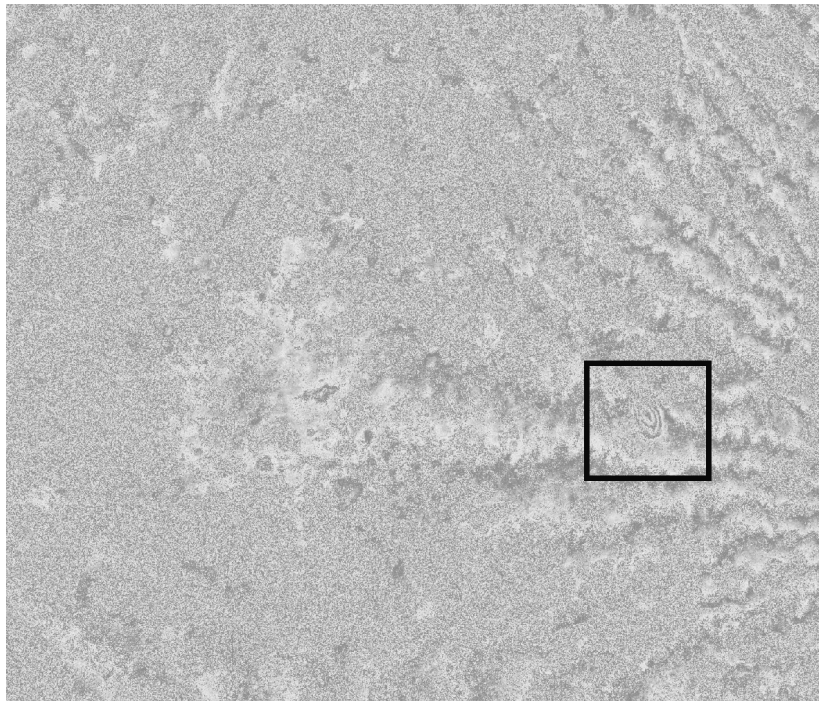
(b) flattened in centre

Figure D.1: Int before & after flattening

Appendix E

SAC CEOS leader file extracted to ASCII

This appendix is included so as to give and indication of the information content of a CEOS header, and also to show how inconsistencies lead to errors in the generation of Gamma parameter files. Note particularly, the errors in the image start time (zero Doppler azimuth time of first pixel).

```
------- LEADER FILE: File Descriptor Record Fixed Segment -------


record sequence number          = 1

1-st record subtype code        = 3F

record type code                = C0

2-nd subtype code               = 12

3-rd subtype code               = 12

length of this record           = 720

ASCII/EBCDIC flag               = A

blanks                          =

fmt control document identifier = CEOS-SAR-CCT

fmt control document rev level  = A

file design descr.  rev letter   = B

generating sw release and rev   = E-SAR-ACS-02

file number                     = 1

file name                       = ERS1.SAR.RAWLEAD

record seq/location type flag   = FSEQ

sequence number location        = 1

sequence number field length    = 4

record code/location type flag  = FTYP

record code location            = 5

record code field length        = 4

record length/loc type flag     = FLGT

record length location          =       9

record length field length      =       4

reserved                        =

reserved segment                =
```

```
Number of data set summary records    =        1
Data set summary record length        =     1886
Number of map projection data records =        0
Map projection record length          =        0
Number of platform pos.  data records =        1
Platform position record length       =     1046
Number of attitude data records       =        0
Attitude data record length           =        0
Number of radiometric data records    =        0
Radiometric record length             =        0
Number of rad.  compensation records  =        0
Radiometric compensation rec.  length =        0
Number of data quality summary records =       0
Data quality summary record length    =        0
Number of data histograms records     =        0
Data histogram record length          =        0
Number of range spectra records       =        0
Range spectra record length           =        0
Number of DEM descriptor records      =        0
DEM descriptor record length          =        0
Number of Radar par.  update records  =        0
Radar par.  update record length      =        0
Number of Annotation data records     =        0
Annotation data record length         =        0
Number of Det.processing records      =        0
Det.processing record length          =        0
Number of Calibration records         =        0
Calibration record length             =        0
Number of GCP records                 =        0
GCP record length                     =        0
spare                                 =
Number of Facility data records       =        2
Facility data record length           =    12288
blanks                                =


------- LEADER FILE: Data Set Summary Record -------


record sequence number                = 2
1-st record subtype code              = A
record type code                      = A
2-nd subtype code                     = 1F
3-rd subtype code                     = 14
length of this record                 = 1886
dss rec_seq_num                       =    1
chan_ind                              =    1
reserved                              =
```

```
scene_number                   = ORBIT=25388-FRAME=4293
input_scene_center_time        = 23-MAY-1996_08:38:40.112
spare                          =
center_lat                     =          -33.9990000
center_long                    =           18.6870000
center_heading                 =
ellipsoid_designator           = GEM6
ellipsoid_semimajor_axis       =         6378.1440000
ellipsoid_semiminor_axis       =         6356.7590000
earth_constant                 =            3.9860044
spare                          =
ellipsoid_j2                   =         1082.2800000
ellipsoid_j3                   =           -2.3000000
ellipsoid_j4                   =           -0.2000000
arvg_height_ellipsoid          =
scene_centre_line_number       =
scene_centre_pixel_number      = 13600    2808
scene_length                   =          110.1056000
scene_width                    =           44.3944800
spare                          =
nchan                          = 0001
spare                          =
mission_identifier             = ERS1
sensor_id_and_mode             = SAR- C-HR-IM-VV
orbit_number                   = 00025388
lat_nadir_center               =  -34.676
long_nadir_center              =   21.951
heading_nadir_center           =  193.615
clock_angel                    =   90.000
incidence_angle_center         =   23.804
radar_freq                     =    5.300
radar_wavelength               =    0.0566000
motion_compensation            = 00
range_pulse_code_specifier     = LINEAR FM CHIRP
range_pulse_amplitude_const    =    1.0000000E+00
range_pulse_amplitude_lin      =    0.0000000E+00
range_pulse_amplitude_quad     =    0.0000000E+00
range_pulse_amplitude_cube     =    0.0000000E+00
range_pulse_amplitude_quart    =    0.0000000E+00
range_pulse_phase_const        =    0.0000000E+00
range_pulse_phase_lin          =    0.0000000E+00
range_pulse_phase_quad         =    2.0889000E+11
range_pulse_phase_cube         =    0.0000000E+00
range_pulse_phase_quart        =
chirp_extraction_index         =   29
spare                          =
```

```
sampling                              =      1.8960000E+01

range_gate_early_edge_start_image     =

range_pulse_length                    =    37.1200000

reserved2                             =

range_compressed_flag                 = NO

reserved3                             =

quantisation_in_bits                  = 00000005

quantizer_descriptor                  = UNIFORM IQ

dc_bias_i                             =         -0.2400000

dc_bias_q                             =         -0.1350000

gain_imbalance                        =          1.0060000

spare                                 =

reserved                              =

antenna_mech_bor                      =         20.3550000

reserved                              =

nominal_prf                           =       1659.9030000

reserved6                             =

satelite_encoded_binary_time          =        551824138

satelite_clock_time                   = 23-MAY-1996 08:04:55.553

satelite_clock_increment              =   3906250

spare                                 =

processing_facility_identifier        =   Hartebeesthoek

processing_system_id                  = ACS

processing_version_id                 = 1

reserved                              =

product_type_id                       = SAR RAW DATA ERS.SAR.RAW

alg_id                                = OMEGA-K

nlooks_az                             =          0.0000000

neff_looks_range                      =          1.0000000

bandwidth_look_az                     =

bandwidth_look_range                  = 15.55

total_look_bandwidth_az               =          0.0000000

total_look_bandwidth_range            = 15.55

w_func_designator_az                  = HAMMING

w_func_designator_range               = HAMMING

data_input_source                     = DLT

nom_res_3db_range                     =

nom_res_az                            =

reserved                              =

a_track_dop_freq_const_early_image    =

a_track_dop_freq_lin_early_image      =

a_track_dop_freq_quad_early_image     =

spare                                 =

c_track_dop_freq_const_early_image    =        621.3480000

c_track_dop_freq_lin_early_image      =      -7884.4280000

c_track_dop_freq_quad_early_image     =
```

```
time_direction_along_pixel         = INCREASE
time_direction_along_line          = INCREASE
a_track_dop_freq_rate_const_early_image=
a_track_dop_freq_rate_lin_early_image  =
a_track_dop_freq_rate_quad_early_image =
spare                              =
c_track_dop_freq_rate_const_early_image= -2115.6290000
c_track_dop_freq_rate_lin_early_image  = 354539.2500000
c_track_dop_freq_rate_quad_early_image =
spare                              =
line_content_indicator             = RANGE
clut_lock_flag                     = NO
autofocussing_flag                 = NO
line_spacing                       =         4.0480000
pixel_spacing_range                =         7.9050000
range_compression_designator       = EXTRACTED CHIRP
spare                              =
zero_dop_range_time_f_pixel        =         5.6075340
zero_dop_range_time_c_pixel        =         5.7556350
zero_dop_range_time_l_pixel        =         5.9037360
zero_dop_az_time_f_pixel           = 23-MAY-1996_08:3
```
zero_dop_az_time_c_pixel   = 8:31.91823-MAY-1   <----Errors
```
zero_dop_az_time_l_pixel           = 996_08:38:40.112
spare                              = 23-MAY-1996_08:38:48.305
number of annotation points        =
spare                              =
line no of first annot.  start      =
pixel no of first annot.  start      =
first annotation text              =
line no of second annotation start  =         00
pixel no of second annotation start = 05199600
second annotation text             = 05 230143 3.110
line no of 3 th annot.  start       = 37260000
pixel no of 3 th annot.  start      = 0000E+04
```
3 th annotation text   = 8.1930000000000   <----Errors
```
line no of 4 th annot.  start       = 00E+00Ea
pixel no of 4 th annot.  start      = rth Cent
4 th annotation text               = red Rotating
line no of 5 th annot.  start       =
pixel no of 5 th annot.  start      =
5 th annotation text               =
line no of 6 th annot.  start       =
pixel no of 6 th annot.  start      =
6 th annotation text               =
line no of 7 th annot.  start       =
```

```
pixel no of 7 th annot.  start            =
7 th annotation text                      =
line no of 8 th annot.  start             =
pixel no of 8 th annot.  start            =
8 th annotation text                      =
line no of 9 th annot.  start             =
pixel no of 9 th annot.  start            =
9 th annotation text                      = 5.5
line no of 10 th annot.  start            = 30132760
pixel no of 10 th annot.  start           = 000000E+
10 th annotation text                     = 06 2.26032184000
line no of 11 th annot.  start            = 0000E+06
pixel no of 11 th annot.  start           = -3.96273

11 th annotation text                     = 2920000000E+06-3      <-----Errors
line no of 12 th annot.  start            = .0816355
pixel no of 12 th annot.  start           = 00000000
12 th annotation text                     = E+03-3.165783830
spare                                     = 000000E+03-6.1140848200000


------- LEADER FILE: Platform Position Data Definition  -------


record sequence number        = 4
1-st record subtype code      = A
record type code              = 1E
2-nd subtype code             = 1F
3-rd subtype code             = 14
length of this record         = 1046
reserved                      =
num_data_points               = 0005
year_of_data_points           = 1996
month_of_data_points          = 0005
day_of_data_points            = 23
day_of_data_points_in_year    = 0143
sec_of_day_of_data            = 3.110372600000000E+04
data_points_time_gap          = 8.193000000000000E+00
ref_coord_sys                 = Earth Centred Rotating
greenwhich_mean_hour_angle    =
a_track_pos_err               =
c_track_pos_err               =
radial_pos_err                =
reserved                      =
++++++++state_vec:  1++++++++++++
pos_x                         =  5.530132760000000E+06
pos_y                         =  2.260321840000000E+06
```

```
pos_z                           = -3.962732920000000E+06
vel_x                           = -3.081635500000000E+03
vel_y                           = -3.165783830000000E+03
vel_z                           = -6.114084820000000E+03
+++++++state_vec:  2+++++++++++
pos_x                           =  5.504670040000000E+06
pos_y                           =  2.234318530000000E+06
pos_z                           = -4.012680830000000E+06
vel_x                           = -3.134056280000000E+03
vel_y                           = -3.181877600000000E+03
vel_z                           = -6.078673690000000E+03
+++++++state_vec:  3+++++++++++
pos_x                           =  5.478778690000000E+06
pos_y                           =  2.208184570000000E+06
pos_z                           = -4.062336810000000E+06
vel_x                           = -3.186266670000000E+03
vel_y                           = -3.197677830000000E+03
vel_z                           = -6.042822630000000E+03
+++++++state_vec:  4+++++++++++
pos_x                           =  5.452460460000000E+06
pos_y                           =  2.181922360000000E+06
pos_z                           = -4.111697270000000E+06
vel_x                           = -3.238262560000000E+03
vel_y                           = -3.213183650000000E+03
vel_z                           = -6.006534310000000E+03
+++++++state_vec:  5+++++++++++
pos_x                           =  5.425717110000000E+06
pos_y                           =  2.155534320000000E+06
pos_z                           = -4.160758630000000E+06
vel_x                           = -3.290039880000000E+03
vel_y                           = -3.228394220000000E+03
vel_z                           = -5.969811440000000E+03



------- LEADER FILE: Facility Related Data -------


- - - - - - - - Facility Record:  (01) -



Can't identify this facility data type:  Facility Related data record General Type
- - - - - - - - Facility Record ended:  - - -


- - - - - - - - Facility Record:  (02) -



Can't identify this facility data type:  FACILITY RELATED DATA RECORD [ESA PCS QUALITY
- - - - - - - - Facility Record ended:  - - -
```

Appendix F

Gamma SAR processing parameter file example

Contains parameters configuring/documenting the SAR Processing

```
title:                      Cape_05715
date:                        1996  5  24
raw_data_start_time:        8  38  31.309
channel/mode:               VV
earth_semi_major_axis:      6378137.0000   m
earth_semi_minor_axis:      6356752.3141   m
scene_center_latitude:      -33.980798    decimal degrees
scene_center_longitude:     18.778584    decimal degrees
track_angle:                -165.155242   degrees
platform_altitude:          797392.5146   m
terrain_height:            0.0000   m
sensor_position_vector:        0.000000      0.000000      797392.514634   m      m       m
sensor_velocity_vector:        7122.759211  0.000000      0.000000        m/s     m/s    m/s
sensor_acceleration_vector:    0.000000     0.000000      0.000000        m/s^2 m/s^2 m/s^2
pulse_repetition_frequency:   1659.903556   Hz
I_bias:                            15.533501
Q_bias:                            15.468819
I_sigma:                           3.332923
Q_sigma:                           3.323242
IQ_corr:                           0.008391
SNR_range_spectrum:       14.254
DAR_doppler:                      0.000   Hz
DAR_snr:                           0.000
doppler_polynomial:    -1.27578e+03  0.00000e+00  0.00000e+00  0.00000e+00    Hz Hz/m Hz/m^2 Hz/m^3
echo_time_delay:                 5.606270e-03   s
receiver_gain:                    -19.0000    dB
calibration_gain:                 -2.8000    dB
near_range_raw:                840358.7318   m
center_range_raw:           862554.6001   m
far_range_raw:              884750.4684   m
near_range_slc:             840347.9492   m
center_range_slc:           859756.9804   m
```

```
far_range_slc:               879173.9174   m
range_pixel_spacing:         7.905919   m
range_resolution:                  13.495   m
sec_range_migration:         OFF
azimuth_deskew:              ON
autofocus_snr:                     71.6033
azimuth_bandwidth_fraction:  0.8000
offset_to_first_echo_to_process:       0   echoes
echoes_to_process:           27200   echoes
range_offset:                      0   samples
range_fft_size:              8192
range_looks:                       1   looks
azimuth_looks:                     1   looks
azimuth_offset:              -0.28495   s
azimuth_pixel_spacing:       4.057588   m
azimuth_resolution:          5.072   m
range_pixels:                      4912   samples
azimuth_pixels:              26141   lines
sensor_latitude:                   -34.640071   decimal degrees
sensor_longitude:                  21.963035   decimal degrees
sensor_track_angle:          -166.393859   decimal degrees
map_coordinate_1:            -33.6452364   19.4781693        0.0000   deg.   deg.   m
map_coordinate_2:            -33.4089277   18.4471193        0.0000   deg.   deg.   m
map_coordinate_3:            -34.5687201   19.1911782        0.0000   deg.   deg.   m
map_coordinate_4:            -34.3296687   18.1463197        0.0000   deg.   deg.   m
map_coordinate_5:            -33.9807976   18.7785839        0.0000   deg.   deg.   m
number_of_state_vectors:     5
time_of_first_state_vector:  31050.00000   s
state_vector_interval:             30.00000   s
state_vector_position_1:     5684736.2750   2425713.9060        -3631991.1970   m   m   m
state_vector_velocity_1:     -2736.7898     -3054.4284          -6332.8321     m/s m/s m/s
state_vector_position_2:     5599691.2570   2333105.1320        -3820173.3290   m   m   m
state_vector_velocity_2:     -2932.4603     -3118.8458          -6211.6279     m/s m/s m/s
state_vector_position_3:     5508814.7420   2238622.0430        -4004628.5590   m   m   m
state_vector_velocity_3:     -3125.5221     -3179.3748          -6084.3926     m/s m/s m/s
state_vector_position_4:     5412188.0470   2142381.9840        -4185177.8480   m   m   m
state_vector_velocity_4:     -3315.7722     -3235.9700          -5951.2536     m/s m/s m/s
state_vector_position_5:     5309898.5320   2044503.5910        -4361646.0640   m   m   m
state_vector_velocity_5:     -3503.0103     -3288.5907          -5812.3436     m/s m/s m/s
```

Appendix G

Example script for running Gamma Modular SAR Processor.

export PATH=$PATH:/mnt/gamma/MSP_v10.5/bin

export PATH=$PATH:/mnt/gamma/ISP_v8.9/display/bin

cp /mnt/gamma/MSP_v10.5/sensors/ERS2_antenna.gain .

cp /mnt/gamma/MSP_v10.5/sensors/ERS2_ESA.par .

#scene title: SAR : 05715

#average reference height of terrain in the scene (m):   0.0000 : 2000

#FFT size for range processing (2048,4096, nominal=8192):   8192 :

#offset (IQ pairs or real samples) to first range sample (<= 0):   0 :

#azimuth prefilter decimation (4 for 4:1 decimation, nominal=1):   1 :

#offset (in echoes) from the start of SAR data to begin processing (>= 0):   0 : 10000

#number of SAR echoes to range compress (<= 18000):   18000 :

#azimuth deskew (ON, OFF): ON:

ERS_proc_ASI LEA_01.001 p05715.slc.par

this produced a partially correct par file. We hacked date, start time & echo delay to first az line from CEOS

header

date: 1996 5 24

raw_data_start_time: 8 38 31.309

echo_time_delay: 5.606270e-03   s

#STEP 4 - Precise orbit extraction - nb file downloaded from internet.

PRC_proc p05715.slc.par PRC_960519_05652_rev2

#STEP 4' - run missing line detector (I used ERS2_ESA.par for this SAC data)
ERS_fix ESA/ESRIN ERS2_ESA.par p05715.slc.par 0 DAT_01.001 05715.fix

#STEP 5 - process SAR data -

./ERS_PROC ERS2_ESA.par 05715 2 10 . . .   4096

Appendix H

Example script for interferogram generation

<u>GAMMA ISP</u>

export PATH=$PATH:/usr/local/gamma/MSP_v10.5/bin

export PATH=$PATH:/usr/local/gamma/ISP_v8.9/display/bin

export PATH=$PATH:/usr/local/gamma/ISP_v8.9/bin

Create soft links to locations of slc files

ln -s /scratch/4/Cape_25388/25388.slc

ln -s /scratch/7/InSAR/Cape_05715/05715.slc

Create ISP SLC parameter files in ISP working directory.

par_MSP /scratch/6/InSAR/Cape_25388/ERS1_ESA.par /scratch/6/InSAR/Cape_25388/p25388.slc.par 25388.slc.par

par_MSP /scratch/8/InSAR/Cape_05715/ERS2_ESA.par /scratch/8/InSAR/Cape_05715/p05715.slc.par 05715.slc.par

REGISTER IMAGES

./INTERF_SLC 05715 25388 2 10 1

Create power images

raspwr 05715_25388.pwr1 2456 1 0

raspwr 05715_25388.pwr2 2456 1 0

Create cor image

#usage: ras_linear <imagefile> <width> [start] [nlines] [pixav] [min_value] [max_value] [LR] [rasf] [inverse] [channel]

ras_linear 05715_25388.cc 2456

Create fused mag and phase.
usage: rasmph <complex> <width> [start] [nlines] [pixavr] [pixavaz] [scale] [exp] [LR] [rasterfile]
rasmph 05715_25388.flt 2456 1 2608 1 1 2.0 0 1

rasmph 05715_25388.int 2456 1 2608 1 1 2.0 0 1

VIEW IMAGES
xv 05715_25388.pwr1.ras &
xv 05715_25388.pwr2.ras &
xv 05715_25388.cc.ras &
xv 05715_25388.flt.ras &
xv 05715_25388.int.ras &

Appendix I

Example script for phase-unwrapping and DEM calculation

GAMMA DIFF & Geo.

export PATH=$PATH:/mnt/gamma/ISP_v8.9/phase/bin

Step 1. Adaptive filtering of the interferogram
usage: adapt_filt <interferogram> <smoothed interferogram> <width> [low_SNR_thr] [filt_width] [xmin] [xmax] [ymin] [ymax]
adapt_filt 05715_25388.flt 05715_25388.flt.sm 2456 0.25 2.5 0 2455 0 2607
rasmph 05715_25388.flt.sm 2456 1 2608 1 1 2.0 0 1
xv 05715_25388.flt.sm.ras &
if step 1 produces a blank image, try reducing the number of processed lines by 10 or so.

Step 2. Masking of regions of low correlation (threshold set here at 0.1) Flag file is created.
usage: corr_flag <corr_file> <flag_file> <width> <corr_thr> [xmin] [xmax] [ymin] [ymax] [border]
corr_flag 05715_25388.cc 05715_25388.flt.sm.flag 2456 0.1
rasbyte 05715_25388.flt.sm.flag 2456
xv 05715_25388.flt.sm.flag.ras &

Step 3. Layover areas are masked - based on backscatter. The threshold is set as a multiple of
the average intensity. Flag file is updated.
neutron 05715_25388.pwr1 05715_25388.flt.sm.flag 2456 20 0 2607
rasbyte 05715_25388.flt.sm.flag 2456
xv 05715_25388.flt.sm.flag.ras &

Step 4. Residue determination. Flag file is updated.
residue 05715_25388.flt.sm 05715_25388.flt.sm.flag 2456 0 2455 0 2607

\# rasbyte 05715_25388.flt.sm.flag 2456

\# xv 05715_25388.flt.sm.flag.ras &

\# Step 5. Residues are connected - max branch length can be set.

\# Here 32 is the default max branch length.

\# usage: tree_gzw <flagfile> <width> [mbl] [xmin] [xmax>] [ymin] [ymax]

tree_gzw 05715_25388.flt.sm.flag 2456 28 0 2455 0 2607

\# Step 6. Manually determine the starting position for phase unwrapping before continuing.

\# Step 7. Phase unwrapping is started at a user defined place

\# usage: grasses <int> <flag> <unw> <width> [xmin] [xmax] [ymin] [ymax] [xinit] [yinit] [init_ph_flag]

grasses 05715_25388.flt.sm 05715_25388.flt.sm.flag 05715_25388.flt.sm.unw 2456 0 2455 0 2607 2121 1986 1

ras_linear 05715_25388.flt.sm.unw 2456

xv 05715_25388.flt.sm.unw.ras &

\# If step 7 fails, you must delete files produced by it before trying again with different parameters:

\# rm *.unw*

\# rm *.flag

\# Step 8. Construction of bridges.

rastree 05715_25388.flt.sm 05715_25388.flt.sm.unw 05715_25388.flt.sm.flag 2456 1 2608 0.25 05715_25388.flt.sm.brid

xv 05715_25388.flt.sm.bridge.ras &

\# Step 9. ASCII bridges file has to be generated manually.

xedit 05715_25388.bridges &

\# Step 10. The bridges are then used to unwrap the phase in connected areas

bridge 05715_25388.flt.sm 05715_25388.flt.sm.flag 05715_25388.flt.sm.unw 05715_25388.bridges 2456 0 2455 0 2607

rastree 05715_25388.flt.sm 05715_25388.flt.sm.unw 05715_25388.flt.sm.flag 2456 1 2608 0.25 05715_25388.flt.sm.brid

xv 05715_25388.flt.sm.bridge.ras &

\# Height map generation:

rasrmg 05715_25388.flt.sm.unw 05715_25388.pwr1 2456

\# The gcp_ras gcp editor doesn't work (related to viewer problem)

\# Manually create a gcp txt file in the form (gcp# rng az hgt)

gcp_phase 05715_25388.flt.sm.unw 05715_25388.off test.gcp 05715_25388.gcp_data2 5

base_ls 25388.slc.par 05715_25388.off 05715_25388.gcp_data2 05715_25388.base 1 4

observe on-screen quality control info.

hgt_map 05715_25388.flt.sm.unw 05715_25388.flt.sm.flag 25388.slc.par 05715_25388.off 05715_25388.base 05715_25388.hgt2 05715_25388.gr2

rashgt 05715_25388.hgt2 05715_25388.pwr1 2456

xv 05715_25388.hgt2.ras &

ORTHONORMALISATION

res_map 05715_25388.hgt2 05715_25388.gr2 05715_25388.pwr2 25388.slc.par 05715_25388.off 05715_25388.rhgt2 05715_25388.rpwr2 05715_25388.slope

rashgt 05715_25388.rhgt2 05715_25388.rpwr2 2456

xv 05715_25388.rhgt2.ras &